AGU ADVANCING EARTH AND SPACE SCIENCE

Earth and Space Science

RESEARCH ARTICLE
10.1029/2021EA001962

Improving the Calibration of the Swiss Plate Geophone Bedload Monitoring System by Filtering Out Seismic Signals From Extraneous Particle Impacts

Tobias Nicollier[1,2], Gilles Antoniazza[1,3], Dieter Rickenmann[1], Arnd Hartlieb[4], and James W. Kirchner[1,2,5]

[1]Swiss Federal Research Institute WSL, Birmensdorf, Switzerland, [2]Department of Environmental System Sciences, ETH Zürich, Zürich, Switzerland, [3]Institute of Earth Surface Dynamics (IDYST), University of Lausanne, Lausanne, Switzerland, [4]Laboratory of Hydraulic and Water Resources Engineering, Technical University of Munich, Obernach, Germany, [5]Department of Earth and Planetary Science, University of California, Berkeley, CA, USA

Abstract The spatio-temporal variability of bedload transport processes poses considerable challenges for bedload monitoring systems. One such system, the Swiss plate geophone (SPG), has been calibrated in several gravel-bed streams using direct sampling techniques. The linear calibration coefficients linking the signal recorded by the SPG system to the transported bedload can vary between different monitoring stations by about a factor of six, for reasons that remain unclear. Recent controlled flume experiments allowed us to identify the grain-size distribution of the transported bedload as a further site-specific factor influencing the signal response of the SPG system, along with the flow velocity and the bed roughness. Additionally, impact tests performed at various field sites suggested that seismic waves generated by impacting particles can propagate over several plates of an SPG array, and thus potentially bias the bedload estimates. To gain an understanding of this phenomenon, we adapted a test flume by installing a partition wall to shield individual sensor plates from impacting particles. We show that the SPG system is sensitive to seismic waves that propagate from particle impacts on neighboring plates or on the concrete bed close to the sensors despite isolating elements. Based on this knowledge, we designed a filter method that uses time-frequency information to identify and eliminate these "apparent" impacts. Finally, we apply the filter to four field calibration datasets and show that it significantly reduces site-to-site differences between calibration coefficients and enables the derivation of a single calibration curve for total bedload at all four sites.

Plain Language Summary Flood-related hazards like bedload transport can potentially constitute a significant threat to human life and infrastructure. The spatio-temporal variability of these processes poses considerable challenges for bedload monitoring systems such as the Swiss plate geophone (SPG). Calibration relationships linking the signal recorded by the SPG system to the transported bedload can vary significantly between different monitoring stations, possibly due to site-specific factors such as the coarseness of the bedload, the flow velocity and the bed roughness. Additionally, impact tests performed at various field sites suggested that seismic waves generated by impacting particles can be detected simultaneously by multiple sensors, and thus potentially bias the bedload estimates. To gain an understanding of this phenomenon, we adapted a test flume by installing a partition wall to shield individual sensor plates from impacting particles. We show that the SPG system is sensitive to seismic waves generated by impacts either on neighboring plates or on the flume bed close to the sensors. Based on this knowledge, we designed a filter method that uses time-frequency information to identify and eliminate these "apparent" impacts. Finally, we apply the filter to four field calibration datasets and show that filtering significantly reduces site-to-site differences between calibration relationships.

Key Points:

- Seismic waves generated by impacting bedload particles can propagate over several plates of the Swiss plate geophone system
- Flume experiments enabled the characterization of signals originating from impacts either on neighboring plates or on the flume bed
- A filter method eliminating apparent impacts was developed and applied to field calibration datasets, improving site-to-site comparisons

Supporting Information:

Supporting Information may be found in the online version of this article.

Correspondence to:

T. Nicollier,
tobias.nicollier@wsl.ch

Citation:

Nicollier, T., Antoniazza, G., Rickenmann, D., Hartlieb, A., & Kirchner, J. W. (2022). Improving the calibration of the Swiss plate geophone bedload monitoring system by filtering out Seismic signals from extraneous particle impacts. *Earth and Space Science*, *9*, e2021EA001962. https://doi.org/10.1029/2021EA001962

Received 17 AUG 2021
Accepted 17 APR 2022

Author Contributions:

Conceptualization: Tobias Nicollier, Dieter Rickenmann
Investigation: Tobias Nicollier, Gilles Antoniazza
Methodology: Tobias Nicollier, Gilles Antoniazza, Arnd Hartlieb
Project Administration: Dieter Rickenmann, James W. Kirchner
Supervision: Dieter Rickenmann, Arnd Hartlieb, James W. Kirchner
Visualization: Tobias Nicollier

1. Introduction

Various climate-related indicators suggest that European Alpine water courses will be substantially altered by climate change (FOEN, 2021; Stoffel et al., 2014). In recent times, more frequent flooding has been observed in several parts of Europe, affecting society as well as ecosystems (e.g., Blöschl et al., 2020). Flood-related hazards like bedload transport pose a significant threat to human life and infrastructure, especially in small alpine catchments (Badoux et al., 2014). However, monitoring and predicting such bedload transport processes

Writing – original draft: Tobias Nicollier, Dieter Rickenmann, James W. Kirchner

still represents a considerable challenge because of their large spatio-temporal variability (e.g., Ancey, 2020; Einstein, 1937; Habersack et al., 2008; Mühlhofer, 1933; Reid et al., 1985; Rickenmann, 2017).

Traditional direct bedload sampling methods such as retention basins, slot samplers or mobile bag samplers (e.g., Helley & Smith, 1971) have a limited resolution in space and time, determined by factors such as the sampler capacity (e.g., Habersack et al., 2017), the flow conditions (e.g., Bunte et al., 2004) or the bed material texture (Camenen et al., 2012). In the last decade or so, more effort was put into the development of indirect bedload surrogate monitoring technologies, in order to overcome some of the limitations of direct methods (Gray et al., 2010; Rickenmann, 2017). This is achieved by using active sensors, such as acoustic Doppler current profilers (aDcp; Le Guern et al., 2021), that emit acoustic signals, or by using passive sensors that record acoustic or elastic waves generated by bedload. Seismometers installed on streambanks (Dietze et al., 2019; Gimbert et al., 2019; Roth et al., 2016) and underwater microphones (Geay et al., 2017; Thorne, 1986) record the signal produced by both the interparticle collisions of moving bedload material and the collision of bedload particles with the bed. Devices such as the Japanese pipe microphone (Mao et al., 2016; Mizuyama, Laronne et al., 2010, Mizuyama, Oda et al., 2010) or the impact plate system equipped with either a microphone, a piezoelectric sensor, or a geophone (e.g., Hilldale et al., 2015; Koshiba et al., 2018; Krein et al., 2008; Kuhnle et al., 2017; Raven et al., 2010; Rickenmann & McArdell, 2007; Wyss et al., 2016c) are intended to record the vibration or sound produced by the elastic impact of particles directly on a metallic structure.

Surrogate monitoring techniques such as these offer many advantages over the traditional direct methods in terms of robustness, spatial coverage and temporal resolution. However, numerous recent studies have demonstrated that concurrent bedload sampling is still indispensable to efficiently calibrate impact plates (Habersack et al., 2017; Kreisler et al., 2017; Nicollier et al., 2021; Rickenmann et al., 2012, 2014), hydrophones (Geay et al., 2017) and pipe microphones (Dell'Agnese et al., 2014; Mao et al., 2016; Mizuyama, Laronne, et al., 2010). Typically, linear or power-law calibration relationships are developed between measured signal properties and bedload transport characteristics. Such calibration equations enable spatio-temporal estimates of bedload fluxes and the detection of the start and end of bedload transport. However, each site must be individually calibrated, because the current bedload surrogate measuring techniques lack generally applicable signal-to-bedload-flux calibration equations that are valid across multiple field sites. A further limitation to the use of surrogate monitoring systems can arise from the bedload transport itself. Seismometers installed on the banks, for instance, have been found to be unable to record bedload transport if the particle size or the impact rate was too low (e.g., Anthony et al., 2018; Barrière, Oth, et al., 2015).

Surrogate monitoring techniques can also be impaired by ambient noise sources. Water turbulence, for example, can significantly reduce the ability of aDcp systems (Conevski et al., 2018), seismometers (Roth et al., 2016) or hydrophones (Geay et al., 2017; Gray et al., 2010) to measure bedload transport. In addition, anthropogenic sources (Barrière, Krein, et al., 2015) and rainfall (Roth et al., 2016) can both generate ground vibrations in a similar frequency band as bedload transport. Recent studies report the successful implementation of time-frequency based methods to increase the signal-to-noise ratio and improve the detectability of bedload particles using pipe hydrophones (Choi et al., 2020) and impact plate systems (Barrière, Krein, et al., 2015; Koshiba & Sumi, 2018).

Among the passive monitoring techniques, the Swiss plate geophone (SPG) system has been deployed and tested in 21 steep gravel-bed streams and rivers, mostly in the European Alps (Rickenmann, 2017). Although the similarities between calibration measurements from various field sites are encouraging, it is not well understood why the site-specific linear calibration coefficients can vary by about a factor of six among different sites, excluding the special case of the ephemeral Nahal Eshtemoa stream (Halfi et al., 2020; Rickenmann & Fritschi, 2017; Rickenmann et al., 2014). Wyss et al. (2016a) found that the flow velocity can matter, with higher flow velocities inducing a weaker signal response. Another important site-dependent factor influencing the signal response is the grain-size distribution (GSD) of the transported bedload (Nicollier et al., 2021): coarser grain mixtures yield stronger signal responses, per unit bedload weight, in the SPG system. SPG systems have typically been assumed to be insensitive to background noise such as water turbulence, because of damping by the elastomer supports for the impact plates, and due to the high threshold value used for impulse counts (Wyss et al., 2016a). However, recent impact tests performed at various field sites suggest that the energy released by an impact on a plate can propagate over several plate lengths and register as false detections across multiple sensors (Antoniazza et al., 2020).

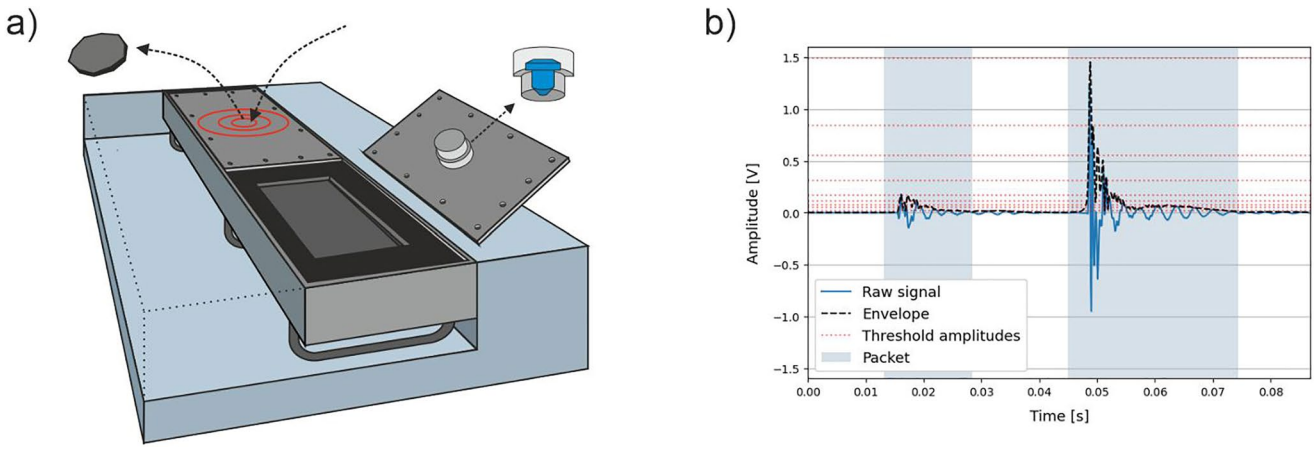

Figure 1. (a) Swiss plate geophone (SPG) array embedded in concrete including two steel plates, each equipped with a uniaxial geophone sensor fixed in a watertight aluminum box attached to the underside of the plate. The plates are acoustically isolated from each other by elastomer elements (black). (b) Example of two packets (light blue area) detected by the SPG system. The start of a packet, as defined by Wyss et al. (2016c), begins 2 ms before the signal envelope crosses the lowest amplitude threshold of 0.0216 V and ends 2 ms after the last crossing of the lowest amplitude threshold of 0.0216 V.

Here, we examine the propagation of seismic waves generated by impacts as a possible noise source affecting the signal response of the SPG system and biasing calibration relationships. We characterize the propagated waves detected by the SPG system using field and flume calibration data, in order to distinguish signal packets originating from measurement artifacts versus real bedload transport. Furthermore, we analyze a set of full-scale controlled flume experiments conducted at the Obernach flume facility (Bavaria, Germany), where we used a partition wall to shield one sensor plate from impacting bedload particles. Finally, we propose a signal processing method that aims to isolate each sensor plate from propagating waves and apply it to field calibration data. Hence, the objectives of this study are (a) to detect and characterize parts of the raw signal (or packets) recorded by the SPG system that originate as impacts occurring beyond each individual plate, (b) to quantify the number of (unwanted) "apparent" packets generated by waves that propagate from these impacts, as a function of the size of the transported bedload material, (c) to develop a filter method that distinguishes real from apparent packets and (d) to show that filtering calibration data from four field sites reduces the differences between the site-specific calibration coefficients, and enables the derivation of a general calibration equation (or signal conversion procedure) valid at all four sites.

2. Methods

2.1. The SPG System

The SPG system consists in a geophone sensor fixed under a steel plate of standard dimensions 492 × 358 × 15 mm (Figure 1a; Rickenmann, 2017). The geophone (GS-20DX by Geospace technologies; www.geospace.com) uses a magnet moving inside an inertial coil (fixed on springs) as an inductive element. The voltage induced by the moving magnet is directly proportional to the vertical velocity resulting from particle impacts on the plate. This raw voltage output is then digitized using an analog-to-digital converter (NI 9205 by National Instruments) connected to a computer located on one of the banks. Typically, a SPG array includes several plates next to each other, acoustically isolated by elastomer elements. The array is either embedded in a concrete sill or fixed at the downstream face of a check dam. A detailed description of the SPG system can be found in Rickenmann et al. (2014).

Due to data storage limitations, field stations usually do not continuously record the full raw 10 kHz geophone signal. Instead, it is typically pre-processed, and summary values, such as the maximum amplitude and the number of impulses, are recorded at one-minute intervals. However, for the relatively short duration of a single calibration measurement, ranging from a few seconds to one hour, the full raw signal is stored for subsequent post-processing. Wyss et al. (2016c) introduced the packet-based amplitude histogram method to derive the size of individual bedload particles from the geophone signal. Wyss et al. (2016c) define a packet (see Figure 1b) as a brief interval, typically lasting 5–30 milliseconds, reflecting a single impact of a particle on a plate; it starts

Table 1
Characteristics of the Amplitude Classes (AC) j

AC (j) (-)	Lower threshold (V)	$A_{m,j}$ (V)	Lower sieve size (mm)	$D_{m,j}$ (mm)
1	0.0216	0.0336	9.5	12.30
2	0.0527	0.0608	16.0	17.40
3	0.0707	0.0894	19.0	21.80
4	0.1130	0.1381	25.0	28.10
5	0.1670	0.2272	31.4	37.60
6	0.3088	0.4112	45.0	53.20
7	0.5489	0.6783	63.0	71.29
8	0.8378	1.1189	80.7	95.49
9	1.4919	1.8453	113.0	127.87
10	2.2760	(3.0442)	144.7	(171.53)

Note. Amplitude classes (AC) j derived from sieve mesh sizes (for classes 1–7) and from Equation (1) according to Wyss et al. (2016c), including mean amplitude $A_{m,j}$ and mean particle diameter $D_{m,j}$. Particles in classes 8–10 were manually sorted on the basis of linearly extrapolated $D_{m,j}$ values. The values of $A_{m,j}$ *and* $D_{m,j}$ for the largest class (10) in brackets are estimates.

2 ms before the signal envelope crosses the lowest amplitude threshold of 0.0216 V and ends 2 ms after the last crossing of the lowest amplitude threshold of 0.0216 V. The signal envelope is computed with the Hilbert transform (Jones et al., 2002), which compensates for the asymmetric offset of the raw seismic signal around the zero-amplitude level. Each packet is then assigned to a predefined amplitude class (AC; Table 1) depending on its maximum amplitude, yielding a packet-based amplitude histogram. Following Wyss et al. (2016c), each AC j is assumed to be representative of a corresponding grain-size class. The following relationship relates the mean amplitude $A_{m,j}$ (V) to the mean particle size $D_{m,j}$ (mm) for each class j:

$$A_{m,j} = 4.6 \cdot 10^{-4} \cdot {D_{m,j}}^{1.71} \quad (1)$$

The grain-size classes are delimited by the size of the meshes used to sieve the bedload samples obtained during field calibration measurements. In the present study, we have extended the seven classes used by Wyss et al. (2016c) to ten classes, to examine in more detail the behavior of larger bedload particles and their effect on the signal response. Wyss et al. (2016c) showed that the packet-based amplitude histogram method provides reasonable estimates of the fractional bedload mass for the Erlenbach calibration measurements. Since 2016, in addition to the summary values, sections of the raw signal corresponding to packets, as well as their time of occurrence, have been stored at multiple field monitoring stations. To facilitate its implementation at the field stations and to limit the required computing power, the filtering method described in this study is based on packet information only.

Calibration coefficients linking the recorded packet rate PACKT to the measured total bedload flux q_b can be obtained from the following power-law regression equation,

$$\mathrm{PACKT} = a \cdot {q_b}^{b} \quad (2)$$

where a is the linear coefficient and b the exponent determined by regression. In Equation (2), q_b is expressed in (kg m^{-1} s^{-1}) and includes all particles with a diameter larger than 9.5 mm, while PACKT is expressed in (packets m^{-1} s^{-1}) and includes all packets with an amplitude larger than 0.0216 V. Because each plate is 0.5 m wide, PACKT equals twice the packet generation rate for an individual plate, and q_b is twice the transport rate (in (kg s^{-1})) measured across the width of each plate. To facilitate comparisons among calibration coefficients a from different field sites, we also consider the linear form ($b = 1$) of Equation (2), which yields calibration coefficients a that are comparable to the linear calibration coefficient k_b with units (kg^{-1}) determined in previous studies employing the SPG system (e.g., Rickenmann et al., 2014; Wyss et al., 2016a).

To determine the coefficient a and exponent b of Equation (2), we used the reduced major axis (RMA) instead of the ordinary least squares fit. RMA regression has the advantage of defining a bivariate relationship with a unique line (Harper, 2014). Our choice of this method assumes that error is present in both the sampled bedload (e.g., due to an incorrect positioning of the sampler) and the recorded signal, which is influenced by the impact location on a given impact plate, the type of particle motion (e.g., rolling, sliding, saltation), and the impact velocity (Rickenmann & McArdell, 2008), all factors that cannot be quantified, particularly under field conditions. Since we use log-log rating plots, we also improved the estimates by applying a bias correction factor, as suggested by Ferguson (1986).

2.2. Seismic Wave Attenuation

Seismic wave attenuation is often quantified using the quality factor Q. The quality factor is dimensionless but material-dependent; it is inversely proportional to the fractional loss of energy per oscillation cycle. Ammon et al. (2020) describe the quality factor as "the ratio of the mass- and spring-related terms to the coefficient of friction, γ. Q has an inverse relationship with attenuation, such that the smaller Q is, the larger is the attenuation. Higher Q indicates that friction has less influence on the mass' motion". More generally, Q increases together

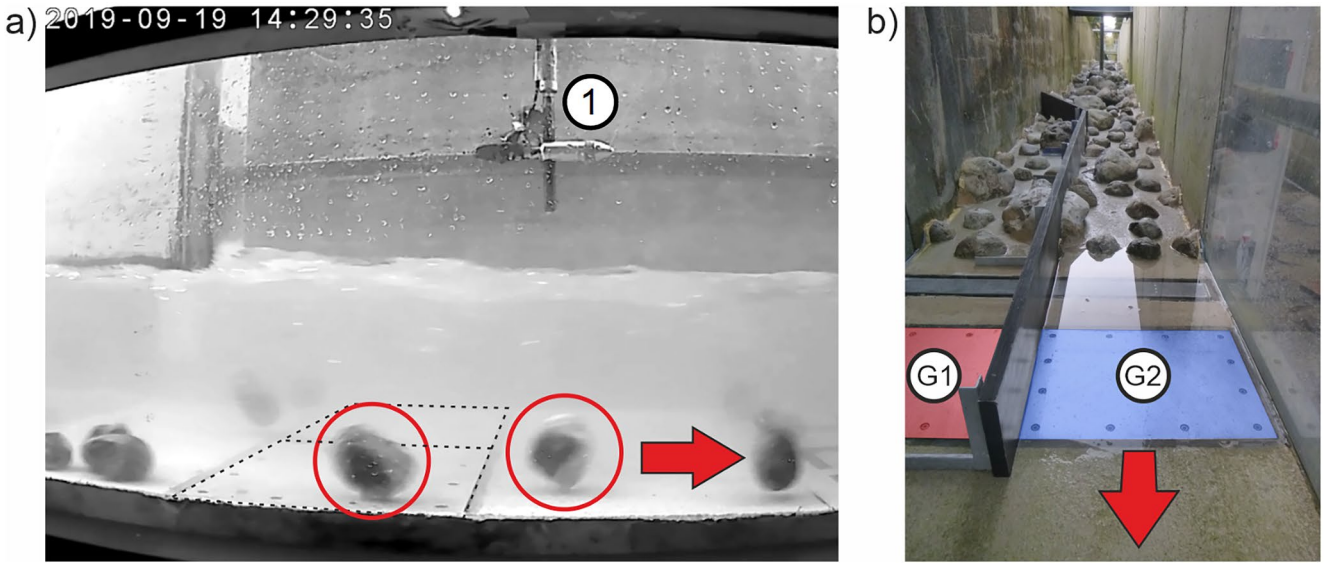

Figure 2. (a) Snapshot of a video recording of a single-grain-size experiment using particles of class $j = 8$ in the original flume setup, without the partition wall. The dashed black line marks the contour of the two impact plates. The left circled particle illustrates an impact on plate G1, which can lead to the recording of one real packet by G1 and one apparent packet by G2. The right circled particle illustrates an impact on the concrete bed, which can lead to the recording of an apparent packet by both sensors. A magnetic-inductive flow meter (1) was used to measure and adjust the flow velocity. (b) Upstream view of the test reach with dimensions of 24 × 1 m. The visible particles were embedded at a fixed position to replicate the bed roughness measured at field sites. During tests, grains were fed into the channel 8 m upstream from the Swiss plate geophon system location. The 4 m–long wooden partition wall and the impact plates are decoupled from each other by a 2 mm gap. The sensor plate G1 is shielded from direct particle impacts. However, both plates can detect impacts on the concrete bed. The red arrows indicate the flow direction.

with the density of the material and the seismic wave speed in the material. Ammon et al. (2020) describe the attenuation of a propagating seismic wave as a function of the distance traveled $A(r)$ using

$$A(r) = A_0 \exp\left(\frac{-f\pi r}{cQ}\right) \tag{3}$$

where A_0 is the initial amplitude, f is the frequency, r is the distance traveled by the wave and c is the wave velocity. The filter method described further in this study is based on three qualitative observations. (a) The longer the travel distance of a seismic wave, the stronger is its attenuation. (b) High frequencies are more effectively attenuated than low frequencies. (c) In the context of a bedload monitoring station, the elastomer used to acoustically isolate the plates from each other attenuates the signal more strongly than does the steel in the supporting structure and the impact plates.

2.3. Packet Classification

The filtering method presented in this study classifies each packet detected by a geophone sensor into the categories "real" and "apparent". While a "real" packet results from a particle impacting on a given plate, an "apparent" packet results from an impact either on a neighboring plate or on the surrounding concrete sill (Figure 2). From Equation (3), one can expect that both the maximal envelope amplitude and the power spectral density of the signal recorded by the SPG will be influenced by the distance between the location of apparent impact and the SPG. Accordingly, the filtering method is based on the packet information listed in the following subsections. We used the stochastic basin-hopping minimization algorithm described by Wales and Doye (1997) and available on SciPy (https://docs.scipy.org) to find the optimal filter parameters for each individual monitoring station as well as for all stations combined. The coefficient of determination R^2 of Equation 2 was used as the objective function for determining the optimal filter parameters.

2.3.1. Maximum Amplitude of the Envelope

Antoniazza et al. (2020) performed impact experiments at the Albula, the Navisence, and the Avançon de Nant field sites in order to quantify the attenuation of signals propagating along a SPG array. The amplitude of the signals recorded on the first neighboring impact plate ($r = 50$ cm) was found to be reduced by 83%–90% relative to the signal recorded on the impacted plate. The maximum amplitude of a given packet $\mathrm{MaxAmp}_{\mathrm{env}}$ is compared here to the maximum amplitude recorded by the two closest neighboring geophones $\mathrm{MaxAmp}_{\mathrm{env,\ neighbor}}$ within a predefined time window (see subsection 2.3.4). If larger amplitudes were recorded by neighboring plates, one can expect that the packet was triggered by a propagating wave originating from outside the considered plate. The amplitude information is retrieved from the envelope that was initially used to delimit the beginning and end of each packet (Wyss et al., 2016c). Compared to the raw signal, the envelope has the advantage of returning the magnitude of the analytical signal and thus better outlines the waveform by omitting the harmonic structure of the signal.

2.3.2. Centroid Frequency

According to the Hertz contact theory, the frequency at which the geophone plate vibrates will depend on the size of the colliding particle (Barrière, Krein, et al., 2015; Bogen & Møen, 2003; Johnson, 1985; Rickenmann, 2017; Thorne, 1986). In previous studies, the frequency spectrum of a packet was characterized by the spectral centroid f_{centroid} (Wyss et al., 2016a). It indicates the center of mass of the spectrum and is computed as

$$f_{\mathrm{centroid}} = \frac{\sum f_n \cdot A_{\mathrm{FFT},n}}{\sum A_{\mathrm{FFT},n}} \tag{4}$$

where $A_{\mathrm{FFT},n}$ (V·s) is the Fourier amplitude (computed with the Fast Fourier Transform) corresponding to the frequency f_n (Hz). Before applying the FFT, the raw data (voltage output by the geophone) in each packet is preprocessed in two steps. First, a 30% cosine taper is applied at the edges of a max. 8 ms time window around the peak amplitude of each packet (see subsection 2.3.4). Second, the signal contained in this time window is zero-padded on either side to reach an optimal number of sample points nFFT. The taper is used to smooth the transition between the packet and the concatenated zeros, and to suppress spectral leakage, which results in a more accurate amplitude spectrum. The value of nFFT was set to 2^7 (12.8 ms) in order to adequately resolve the amplitude spectrum of the raw signal contained in the max. 8 ms time window. The single-sided Fourier transform of the processed packet is then computed in order to extract the A_{FFT} and derive the f_{centroid} (Equation 4). For a given Q, high frequencies will be more rapidly attenuated than low frequencies along the travel path of a seismic wave (Equation 3). Here we take advantage of this phenomenon and use f_{centroid} as threshold to define whether a packet-triggering impact took place on a given plate.

2.3.3. Peak Frequency

A further characteristic of the packet's power spectrum used to classify packets is the peak frequency f_{peak}. f_{peak} is the frequency with the largest amplitude $A_{\mathrm{FFT},n}$ of the single-sided Fourier transform. Real packets are characterized by high f_{peak} values (>1,500 Hz) for a large range of grain sizes. This enables a straightforward classification of packets based on a unique threshold. f_{peak} is implemented in the filtering method as secondary step aiming to classify overlapping packets, that is, packets having an amplitude smaller than the amplitude of the signal recorded by neighboring sensors.

2.3.4. Time Window

Both the comparison of the amplitude with the neighboring signal channel traces and the spectral analysis are carried out within a time window of max. 8 ms around the maximum amplitude of each packet. This time window contains the first arrival waveform. In case the packet duration is shorter than 8 ms, the window is reduced to the length of the packet. The aim of this window is twofold. First, it usually avoids overlapping two packets generated close enough in time but on two different plates. Second, in the words of Barrière, Krein, et al. (2015), "when a sediment particle impacts on the plate, the amplitude and frequency of the first arrival waveform are the two fundamental properties related to the force that the bedload imposes on the plate and the contact time defined as the duration over which the applied impact force is non-zero". Focusing on the first arrival waveform results in a more accurate evaluation of the high-frequency content of the packet.

Note that in previous studies, the traces recorded by the geophones of an SPG array have always been analyzed individually. The novel strategy presented in this study analyzes multiple geophone traces simultaneously, similar to traditional reflection or refraction seismic surveys.

2.3.5. Continuous Wavelet Transform

We attempted to develop a filter method based on the continuous wavelet transform (CWT) as a summary of the time-frequency information of each packet. The CWT was introduced in the field of seismic processing by Goupillaudet al. (1984) and was applied to bedload measurements by Barrière, Krein, et al. (2015). The advantage of the CWT over the more common FFT is its flexible time–frequency resolution. The CWT is computed with the integral over time of the signal multiplied by scaled and shifted versions of a function called the mother wavelet (Kristeková et al., 2006). The CWT was implemented in the filtering method using the tf_misfit package available on Obspy. As suggested by Barrière, Krein, et al. (2015), we used the complex Morlet wavelet as the mother wavelet. However, the CWT is computationally more demanding than the FFT and requires too much buffer memory to be applied in real time at monitoring stations when transport rates are high. Additionally the FFT proved to be accurate enough to retrieve the necessary information from the power spectral density of the signal. Nonetheless we continue to use the CWT as a powerful tool to visualize and better understand the time-frequency evolution (i.e., the spectrogram) of each packet.

2.4. Controlled Flume Experiments

The idea for the filter design comes from controlled experiments conducted at the outdoor flume facility of the Oskar von Miller institute of TU Munich in Obernach, Germany. At this facility, we reconstructed the bed characteristics of the Albula, Navisence, and Avançon de Nant field sites, one after another, in a test reach with dimensions of 24 × 1 m equipped with two impact plates (Figure 2). Each site reconstruction used bedload material collected during field calibration measurements, and we adjusted the flow velocity, flow depth, and bed roughness to match those field observations. A detailed description of the original flume set-up and the performed experiments can be found in Nicollier et al. (2020). In the present study, we took advantage of the flume to (a) characterize the effect of wave propagation as a function of the grain size and (b) test the filter method. In a first stage, the original set-up was modified and a partition wall was installed in the center of the flume, guiding all of the transported bedload particles over a single plate (plate G2; Figure 2b). The non-impacted plate, G1, served as a reference to characterize apparent packets. Single-grain-size experiments were run with a fixed number of grains for each of the ten particle-size classes, resulting in a total of 51 runs in the modified setup (Tables 1, and 3). The flow velocity was set to 3 m/s to facilitate the transport through the narrower flume section and the bed slope was 4%. In a second stage, after having defined an optimal filter, we applied it to the entire data set collected during a series of single-grain-size experiments performed in the original flume set-up between 2018 and 2020 (1,095 runs in total, all without the partition wall). Videos recorded at 120 fps during these experiments were used as a supplementary source of information to identify the location of impacts and to help classifying the generated packets (Figure 2a).

To illustrate the increasing importance of energy propagation with increasing particle diameter during these flume experiments, we use a further calibration coefficient. The coefficient $\alpha_{\mathrm{tot},j}$, as defined by Wyss et al. (2016b), compares as follows the total number of recorded packets $\mathrm{PACK}_{\mathrm{tot}}$ having a maximum envelope amplitude larger than 0.0216 V to the total number of particles N_j fed into the flume for a given grain-size class j:

$$\alpha_{\mathrm{tot},j} = \frac{\mathrm{PACK}_{\mathrm{tot}}}{N_j} \tag{5}$$

Ideally, $\alpha_{\mathrm{tot},j}$ should equal one. Values lower than one indicate missed particle detections, while values greater than one indicate the presence of either particles impacting multiple times a plate, or apparent packets.

Table 2
Channel and Flow Characteristics From In Situ Measurements Made During the Calibration Campaigns at the Four Field Sites

Field Site	Location (canton)	Bed Slope (%)[a]	Flow Velocity V_w (m/s)[b]	No. Plates	Year	Technique	No. of Samples
Albula[c]	Tiefencastel (Grisons)	0.7	2.6	30	2018	crane-mounted net sampler	51
Navisence[c]	Zinal (Valais)	3	3.2	12	2019	crane-mounted net sampler	80
Avançon de Nant[d]	Les Plans-sur-Bex (Vaud)	4	1.3	10	2019/2020	manual basket sampler	55
Erlenbach[e]	Alpthal (Schwyz)	16	5	2	Since 2009	automatic basket sampler	123

Note. The year of the field calibration campaigns, the sampling technique and the number of collected samples are indicated.

[a]Gradient measured upstream of the site. [b]Depth-averaged mean flow velocities measured during the calibration measurements. [c]More information available in Nicollier et al. (2021). [d]More information available in Antoniazza et al. (2022). [e]More information available in for example, Rickenmann et al. (2012), Wyss et al. (2016b), Rickenmann et al. (2018).

2.5. Field Calibration

After having defined the general structure of the filter, the optimal filter parameters were obtained using calibration data collected at four Swiss bedload monitoring stations equipped with the SPG system (Table 2). The Albula, the Navisence, and the Avançon de Nant stations were all calibrated and subsequently replicated in the flume. The extensive field calibration data set from the Erlenbach site was also included in this analysis, in order to test the filter method under different channel and flow characteristics. A calibration consists of the following steps: (a) direct sampling downstream of an impact plate using one of the listed techniques (Table 2), (b) synchronous recording of the raw geophone signal, (c) sieving and weighing the sample according to the ten sieve classes presented in Table 1, (d) comparing both the fractional and the total bedload mass of each sample to the packet-based amplitude histogram data to derive the corresponding calibration coefficient a (Equation 2). A more detailed description of the procedure is reported in Supporting Information S1. This study focuses on the calibrations for the total bedload mass; the calibrations for individual size classes will be the focus of an upcoming paper.

3. Results

3.1. Identification of Wave Propagation in Flume and Field Data

By synchronizing the videos and the seismic traces recorded during the flume experiments performed without the partition wall, we were able to make a first step toward packet classification. The following observations can be made from the example shown in Figure 3. (a) Within the first 0.06 s, Figure 3 shows three impacts on the concrete in the vicinity of the SPG array, detected by both sensors as packets with similarly low amplitudes, and f_{peak} and $f_{centroid}$ values below 900 Hz. (b) Between 0.08 and 0.11 s, and again between 0.17 and 0.19 s, Figure 3 shows impacts on plate G2 and plate G1, respectively. Both impacts are detected by the impacted sensor plate as real packets with f_{peak} and $f_{centroid}$ ranging from 1,300 to 2,000 Hz. (c) These same two impacts are detected by the neighboring sensor plate as apparent packets with f_{peak} and $f_{centroid}$ values ranging from 250 to 1,000 Hz. The attenuation of the high frequencies is visible in the spectrograms of these packets, obtained using the CWT (Figures 3b and 3d). Finally, (d) the maximum amplitude of the real packets is about three times larger than the maximum amplitude of the corresponding apparent packets. Note that these real and apparent packets were also independently determined from the video traces.

The flume is equipped with only two impact plates, whereas field stations can include up to 72 plates (Hilldale et al., 2015). The examples from the Navisence site (Figure 4) illustrate the increasing significance of seismic wave propagation with the number of plates. Note that the exact impact location cannot be verified in the field. Therefore, the examples in Figure 4 only serve as illustrations of the occurrence of wave propagation, and do not constrain the filter design. In Figure 4b, the impact on plate G7 generated an excursion of the signal of about 3.2 V (equivalent to a particle with 177 mm diameter) and was detected by 11 out of 12 plates along the 6 m-long transect. In Figure 4c, all 12 plates have detected the same propagating seismic wave. The parabolic shift of the arrival time and the regular shape of the signal suggest that the impact took place on the concrete in the vicinity of G3. These two field examples are also consistent with the packet characteristics described in Figure 3: impacts on a plate generate centroid and peak frequencies exceeding ~1,000 Hz and maximum amplitudes that are much

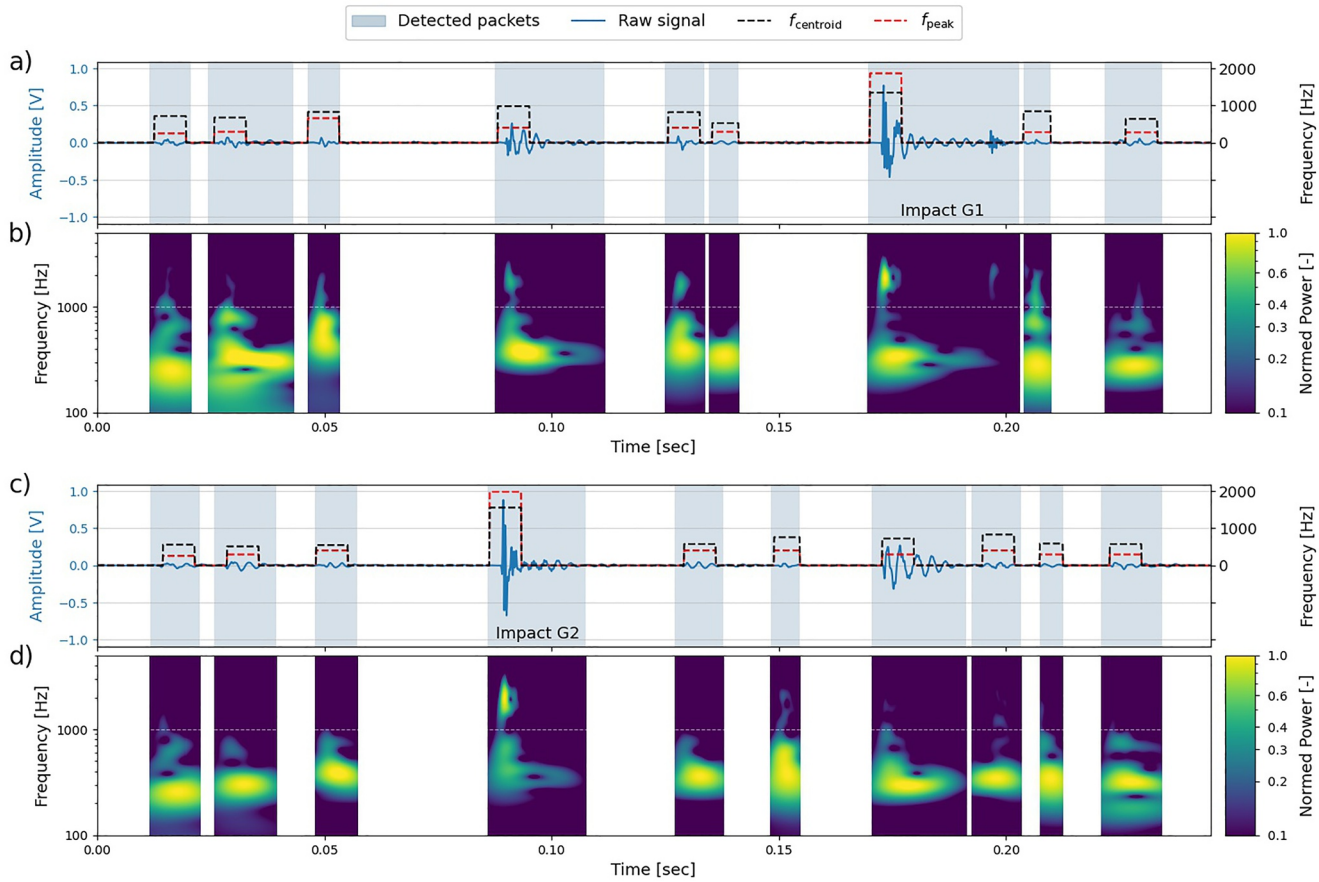

Figure 3. Raw signal (blue lines) recorded by the impact plates (a) G1 and (c) G2 during single-grain-size flume experiments with particles of class $j = 6$. The dashed black lines indicate the centroid frequency within the maximum 8 ms-long time window around the maximum amplitude of each packet, and the dashed red lines indicate the peak frequency within the same time window. In (b) and (d) the spectrogram derived using the continuous wavelet transform is shown for each sensor and each packet. Each spectrogram section is normed with the highest power detected for the corresponding packet, in order to improve the readability of the low-amplitude packets.

greater than those on adjacent plates, whereas impacts on the concrete generate lower peak frequencies, and a more uniform distribution of maximum amplitudes across the plates. Finally, note that all the packets originating from the same impacts do overlap.

3.2. Characterization of Real and Apparent Packets

Results from the single-grain-size flume experiments conducted with the partition wall show that the number of packets recorded by the non-impacted plate (G1) increases together with the particle size (Table 3; Figure 5). While particles of the three smallest classes remained undetected by G1, the largest particles ($j = 10$) generated almost as many packets on G1 as on G2. Also note that the number of recorded packets per particle ($\alpha_{tot,j}$) increases for both sensors with increasing $D_{m,j}$ (Table 3). $\alpha_{tot,j}$ values larger than 1 signify that multiple impacts are being identified per particle. With increasing particle size, the maximum centroid frequency of packets decreases and the maximum amplitude increases (Figure 5), consistent with the Hertz contact theory (Barrière, Krein, et al., 2015). In general, the packets detected by G1 appear to have lower amplitude and frequency values than those recorded by G2. Still, the packet characteristics of the two sensors overlap over a significant area of the amplitude-frequency plots (Figure 5). With the help of video material, it was found that these overlapping packets originate from impacts on the concrete bed. One must therefore keep in mind that the partition wall does not prevent seismic waves generated by impacts on the concrete bed from reaching both the shielded plate G1 and the unshielded plate G2.

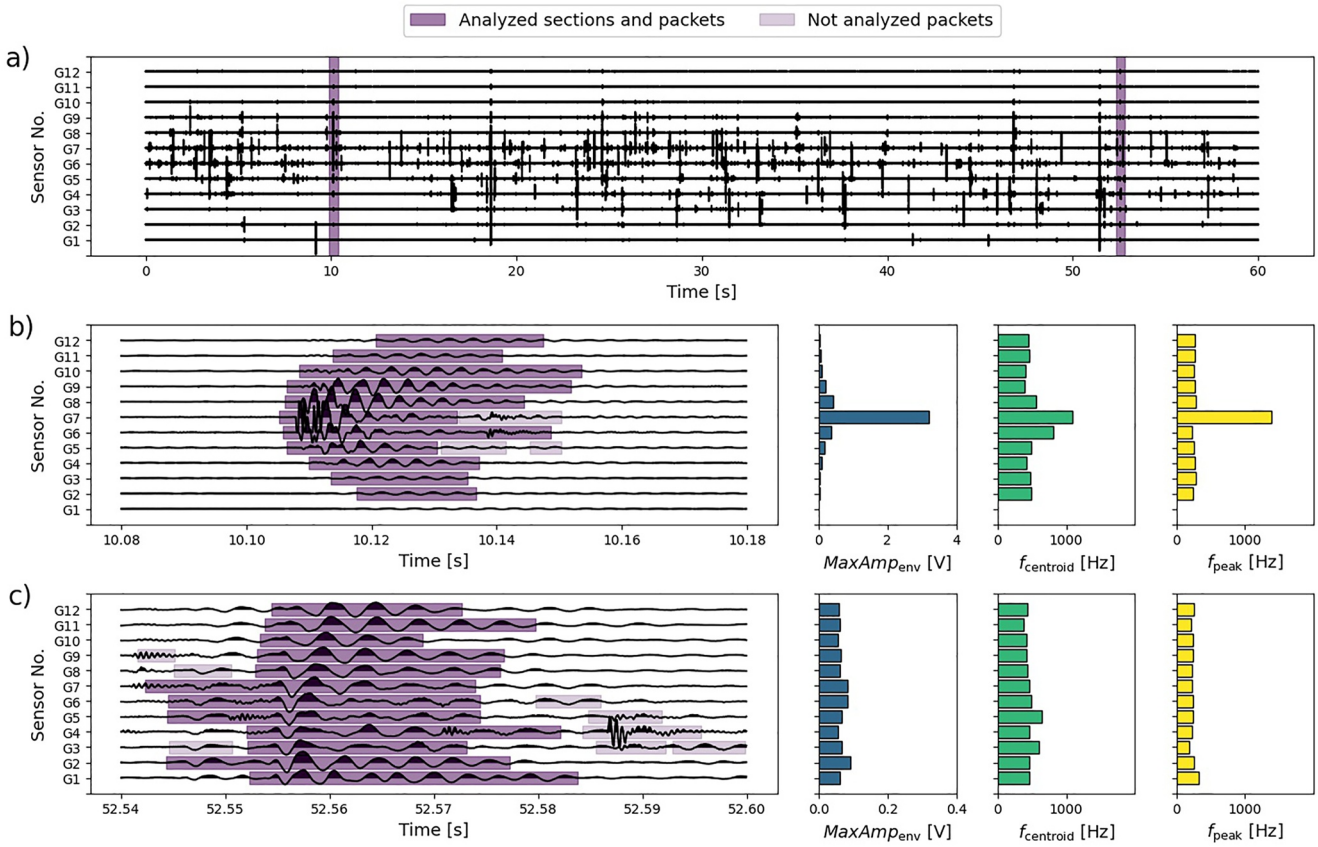

Figure 4. (a) Raw signal recorded by the 12 impact plates during a calibration measurement at the Navisence site (Table 2). The two purple stripes mark the time sections depicted in (b) and (c). Characterization of packets generated by (b) an impact on plate G7 and (c) an impact on the concrete sill close to the right bank. The packets identified by the automated algorithm that are analyzed in the subplots on the right are marked in bright purple. The packets that are ignored are marked in faded purple. $\text{MaxAmp}_{\text{env}}$ is the maximum amplitude of the packet's envelope, and f_{centroid} and f_{peak} are the centroid and peak frequencies, respectively.

We now merge all the single-grain-size experiments conducted with the modified set-up to illustrate the packet characteristics for heterogeneous grain mixtures (under the assumption that any grain-size interactions are minor). In Figure 6, we define real packets as packets recorded by the unshielded sensor (G2; blue dots) that do not lie in the areas of the amplitude-frequency plots shown in Figure 6 occupied by packets recorded by the shielded sensor (G1; red dots). The three types of packet information listed in subsections 2.3.1, 2.3.2 and 2.3.3 help to distinguish real from apparent packets, namely the maximum envelope amplitude ($\text{MaxAmp}_{\text{env}}$) as well as the maximum envelope amplitude recorded by the two closest neighboring geophones ($\text{MaxAmp}_{\text{env, neighbor}}$), the centroid frequency f_{centroid}, and the peak frequency f_{peak}. While $\text{MaxAmp}_{\text{env, neighbor}}$ and f_{centroid} are efficient criteria over the whole range of $\text{MaxAmp}_{\text{env}}$ values (Figures 6a and 6b), f_{peak} shows more overlap between G1 and G2 packets for lower $\text{MaxAmp}_{\text{env}}$ values, and returns stable high frequency values over a large range of $\text{MaxAmp}_{\text{env}}$ values (Figure 6c).

To extrapolate the filter to field data, the signal responses of SPG systems in the field need to be similar to the signal response observed during the flume experiments. This can be examined using density histograms of the three types of packet information. In general, $\text{MaxAmp}_{\text{env, neighbor}}$ (Figure 7, column 1), f_{centroid} (Figure 7, column 2) and f_{peak} values (Figure 7, column 3) recorded during the flume experiments correlate well with the field data. Only the $\text{MaxAmp}_{\text{env, neighbor}}$ values from the Erlenbach data are more scattered than the values from the flume (Figure 7e, column 1). There, the propagating signal appears to be more strongly attenuated, which leads to larger differences between $\text{MaxAmp}_{\text{env}}$ and $\text{MaxAmp}_{\text{env, neighbor}}$. Table 4.

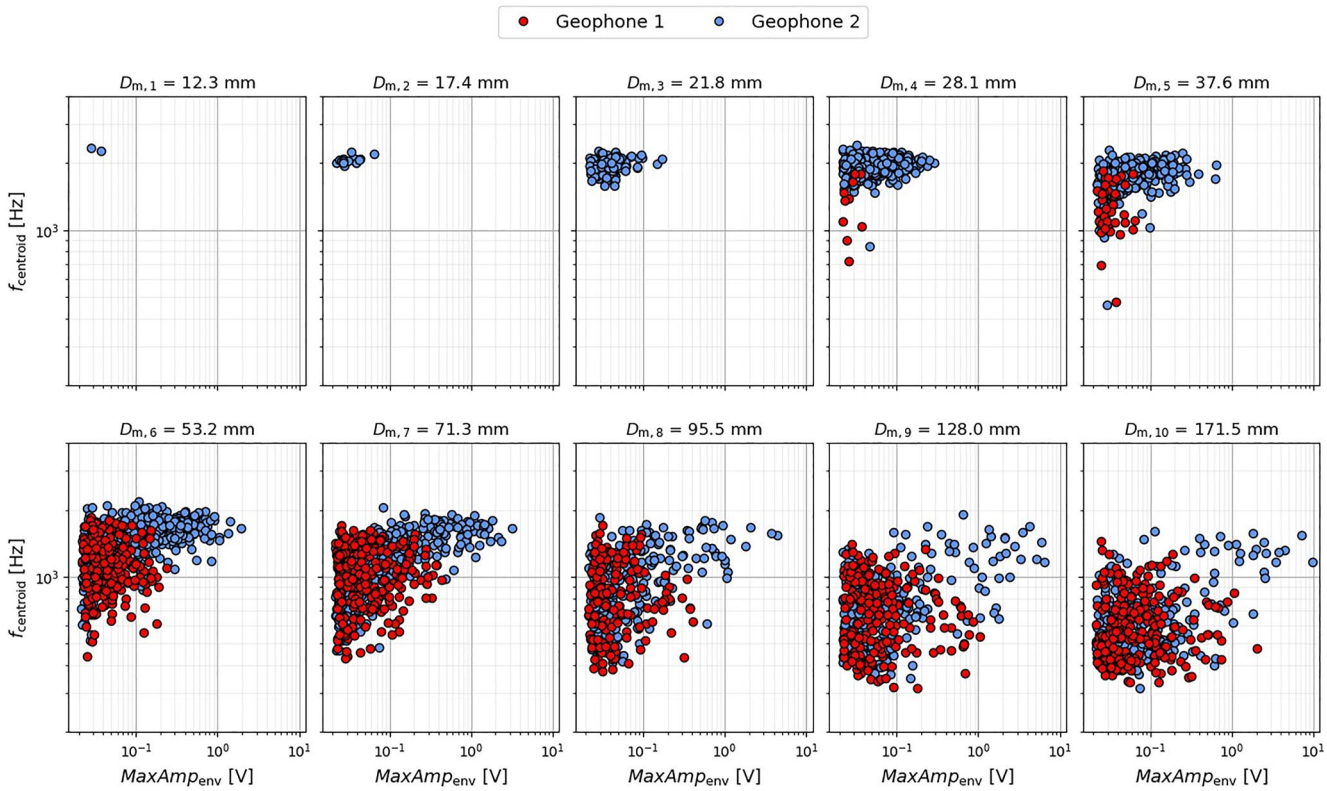

Figure 5. Centroid frequency $f_{centroid}$ as a function of the maximum envelope amplitude $MaxAmp_{env}$ for each packet detected during the single-grain-size experiments conducted using the partition wall (Figure 2b). Each dot corresponds to one packet. The red and blue dots indicate packets recorded by the shielded plate (G1) and the unshielded plate (G2), respectively.

3.3. Filter Parameters

By considering the findings presented in the previous section, we can now design the filter. Each packet recorded by an impact plate is classified as "real" if either of the two criteria applies. The first criterion is that the maximum amplitude recorded on one plate exceeds the maximum amplitude on both adjacent plates (or on the one adjacent plate, if the considered plate is located at the end of an SPG array) by a factor p_1, and the centroid frequency exceeds a specified exponential function of the maximum amplitude (because both will vary with the size of the impacting particle):

$$\textit{Criterion 1:} \quad \mathrm{MaxAmp}_{env} > p_1 \cdot \mathrm{MaxAmp}_{env,neighbor} \;\&\; f_{centroid} > f_1 \cdot e^{(\exp_{coeff} \cdot \mathrm{MaxAmp}_{env})}$$

The second criterion is that the maximum amplitude recorded on one plate exceeds the maximum amplitude on adjacent plates by a different factor p_2, and the peak frequency exceeds a value f_2:

$$\textit{Criterion 2:} \quad \mathrm{MaxAmp}_{env} > p_2 \cdot \mathrm{MaxAmp}_{env,neighbor} \;\&\; f_{peak} > f_2$$

The best values for the filter coefficients p_1, p_2, f_1, f_2 and $\exp_{coeff}$ (Table 4) were defined for various station configurations after multiple runs of the basin-hopping algorithm (as described in Section 2.3) optimizing the coefficient of determination R^2 of Equation 2. This was done using the calibration data from the four field sites where both SPG data measurements and direct bedload samples were collected. The value of coefficient p_1 was constrained to be greater than or equal to 1, to ensure that *Criterion 1* excludes packets resulting from impacts on neighboring plates. The $f_{centroid}$ threshold was set as an exponential function in order to best reproduce the boundary line between the domain where G1 and G2 packets (visually) overlap in Figure 6b, and the domain where they do not. The value of coefficient p_2 in *Criterion 2* is constrained to be less than one in order to accommodate

Table 3
Quantitative Evaluation of the Single-Grain-Size Experiments Conducted in the Modified Flume Set-Up Including the Partition Wall (Figure 5)

Grain-Size Class j	1	2	3	4	5	6	7	8	9	10
$D_{m,j}$	12.3	17.4	21.8	28.1	37.6	53.2	71.3	95.5	128	171.5
No. Repetitions	5	5	5	7	5	5	5	5	5	4
N_j	500	500	400	462	200	200	125	50	25	23
$\alpha_{tot,G1,j}$	0	0	0	0.02	0.20	1.08	2.00	3.46	8.12	10.00
$\alpha_{tot,G2,j}$	0	0.03	0.27	0.89	1.43	2.30	2.99	4.80	10.44	12.30
$PACK_{G1}/PACK_{tot}$	0	0	0	0.02	0.12	0.32	0.40	0.42	0.44	0.45

Note. For each grain-size class j, the following information is listed: the mean particle diameter ($D_{m,j}$), the number of experimental runs (No. repetitions), the number of grains summed over all repetitions (N_j), the average number of recorded packets per particle by each sensor ($\alpha_{tot,G1,j}$ and $\alpha_{tot,G2,j}$), and the proportion of packets recorded by the shielded sensor G1 ($PACK_{G1}/PACK_{tot}$).

some ambiguity in the recorded amplitudes, thus facilitating the classification of impacts with less marked signatures, for example, impacts close to the edge of a plate. An illustration of the frequency thresholds can be found in Figure 7.

3.4. Filtering Flume and Field Data

Figure 8 illustrates the effect of each criterion (as well as of their combination) on the data recorded during the flume experiments conducted with the partition wall. Ideally, all packets recorded by the shielded sensor G1, which are apparent packets, should be filtered out through the application of the two criteria. Sensor G2 records both real and apparent packets, although it is difficult to define the exact proportion of each type of packet (see Section 3.2). *Criterion 1* filters out all the packets recorded by the shielded sensor G1 and 71.5% of the packets recorded by the unshielded sensor G2. *Criterion 2* misses 3.9% of the packets recorded by sensor G1, all with $MaxAmp_{env} < 0.1$ V, but filters out significantly less packets recorded by sensor G2 (47.7%). The combination of both criteria result in the removal of 42.6% of all the packets recorded by G2.

Figure 9 shows the application of the calibrated filter to the time series shown in Figure 3. One can notice that the two real packets originating from direct impacts on plate G2 (between 0.08 and 0.11 s) and plate G1 (between

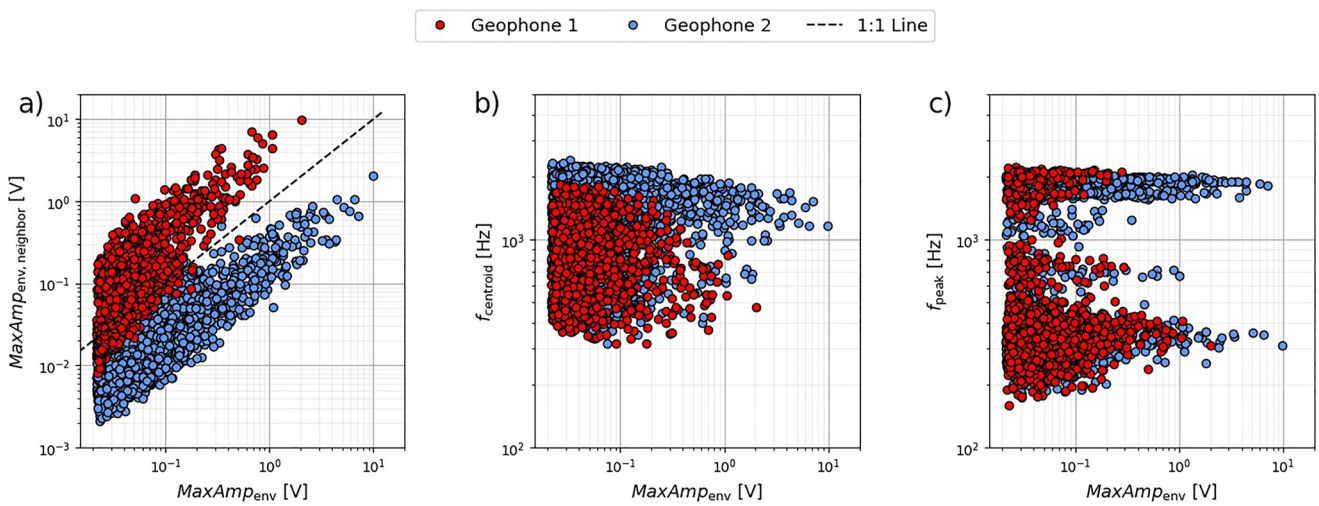

Figure 6. Illustration of all three packet attributes implemented in the filter method after having merged the single-grain-size experiments that used the partition wall (Figure 5). The panels show the relationships between the maximum amplitude of each packet's envelope $MaxAmp_{env}$ and (a) the maximum envelope amplitude of the closest neighboring sensor plates $MaxAmp_{env,\ neighbor}$, (b) the centroid frequency $f_{centroid}$ and (c) the peak frequency f_{peak}. Note that points lying on the dashed 1:1 line in (a) correspond to packets having the same maximum amplitude recorded by the two sensors.

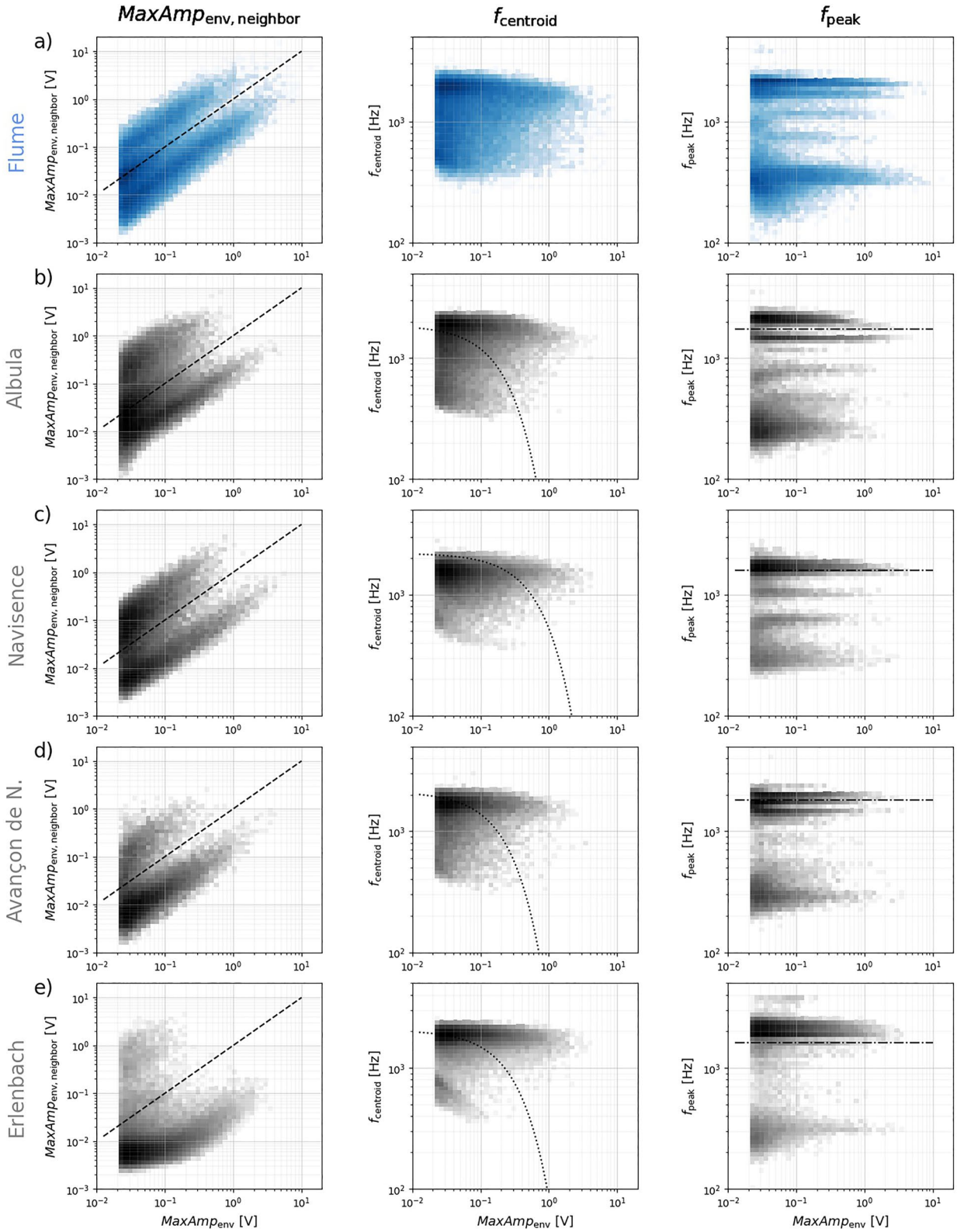
MaxAmp env, neighbor
f centroid
f peak
a)
b)
c)
d)
e)
Flume
Albula
Navisence
Avançon de N.
Erlenbach
MaxAmp env, neighbor [V]
f centroid [Hz]
f peak [Hz]
MaxAmp env [V]

Figure 7.

Table 4
List of the Best Filter Coefficients

Stations	Criterion 1			Criterion 2	
	p_1 (-)	f_1 (Hz)	$\exp_{coeff}$ (-)	p_2 (-)	f_2 (Hz)
Albula	1.56	1,867	−4.51	0.31	1,728
Navisence	1.33	2196	−1.43	0.31	1,593
Avançon de Nant	1.43	2123	−4.28	0.74	1,817
Erlenbach	1.48	2046	−3.19	0.77	1,611
3 stations[a]	1.57	2017	−2.92	0.35	1,616
4 stations[b]	1.75	2390	−3.44	0.37	1,662

Note. The filter coefficients p_1, p_2, f_1, f_2 *and* $\exp_{coeff}$ were estimated by using the basin-hopping algorithm, optimizing the coefficient of determination R^2 of Equation 2 for various station configurations.

[a]Includes the following three stations: Albula, Navisence, and Avançon de Nant.

[b]Includes the following four stations: Albula, Navisence, Avançon de Nant, and Erlenbach.

0.17 and 0.19 s) have been successfully identified (Figures 9a and 9b). Additionally, packet pairs generated by impacts on the concrete were correctly classified as "apparent". Applying the filter to the raw signals recorded during all of the single-grain-size flume experiments (without the partition wall) provides further information on the number of apparent packets generated by each grain-size class. The mean $\alpha_{tot,j}$ values, that is, the number of packets generated by a single particle, for both unfiltered ($\alpha_{tot,all,j}$) and filtered ($\alpha_{tot,real,j}$) data, begin to diverge at class $j = 4$ (Figure 9c). This is consistent with the detection of apparent packets beginning at $j = 4$ in the partitioned wall flume experiment (Figure 5). Note that for size classes $j = 9$ and 10, less than 10% of the packets remain after filtering, implying that over 90% of the packets generated by these size classes are "apparent" rather than real. Interestingly, the filtering process results in a relatively stable signal response over the grain-size classes $j = 4$–10, with $\alpha_{tot,real,j}$ values ranging from 0.78 to 1.68. Before the filter was applied, $\alpha_{tot,all,j}$ varied by more than a factor of 15, ranging from 1.1 to 18 for the same seven grain-size classes.

Finally, we apply the filter to the calibration data from the four field sites, using the optimal parameters listed in Table 4. While the power-law regression lines fit the data better (Figure 10), the linear relations are useful to evaluate the effect of the filtering (Table 5). The following observations can be made. First, 48%–57% of the packets recorded at the Albula, Navisence and, Avançon de Nant sites were removed through the filtering procedure (i.e., identified as apparent packets). At the Erlenbach site, only 20% of the packets were removed. Second, as the example of the Albula data set shows, filtering may not necessarily improve the calibration relation at individual stations. Third, the linear coefficient a in Equation 2 has a reduced variability after application of the filter. Before filtering, a varies by a factor of 3.25, and after filtering, a varies by a factor of 2.12, showing that the Erlenbach station still records significantly less packets than the other stations for a given bedload flux. Last, filtering improves the coefficient of determination R^2 of the global calibration relation valid for all four sites from 0.80 to 0.91. However, R^2 does not increase after filtering when considering only three stations, excluding the Erlenbach site, whose channel and flow characteristics strongly differ from the other sites (Table 2).

4. Discussion

4.1. Importance of Filtering

The reasons for the six-fold site-to-site variation in the linear calibration coefficients linking SPG signals to the transported bedload (e.g., Rickenmann et al., 2014; Rickenmann & Fritschi, 2017) are gradually becoming clearer. Wyss et al. (2016a) found that in flume experiments, higher flow velocities result in fewer packets per unit mass being recorded, due to longer saltation lengths and flatter impact angles. Another important factor influencing the signal response was found to be the GSD of the transported bedload (Nicollier et al., 2021). By comparing results from field and flume calibration measurements, Nicollier et al. (2021) found that the coarser a grain mixture is, the more packets are recorded by the SPG system per unit weight, mainly in the four smallest ACs (Table 4). The findings presented in the present study support the hypothesis that the effect of the GSD on the signal response is related to the phenomenon of wave propagation. The field data analyzed here demonstrate that strong impacts can generate seismic waves that propagate far enough to be detected by multiple sensors (Figure 4). Consequently, the coarser the mobilized bedload is, the more packets are being generated by waves propagating from outside an individual plate. Unfortunately the GSD will typically be unknown in a given stream, unless bedload samples are collected or unless it can be inferred from the SPG signals themselves. A further

Figure 7. Density histograms of all three packet attributes implemented in the filter method using a resolution of 50 × 50 bins. The panels show the amplitude and frequency information for all the packets detected during single-grain-size flume experiments (a), without the partition wall, reproducing the Albula, the Navisence, and the Avançon de Nant field sites (Nicollier et al., 2021). The same amplitude and frequency information is shown for the field calibration measurements conducted at the Albula (b), the Navisence (c), the Avançon de Nant (d), and the Erlenbach site (e). Each dashed line in the panels of the first column is the 1:1 line. Each dotted line in the panels of the second column illustrates the $f_{centroid}$ threshold derived for the given station (Table 4). Each dash-dotted line in the panels of the third column illustrates the f_{peak} threshold derived for the given station (Table 4).

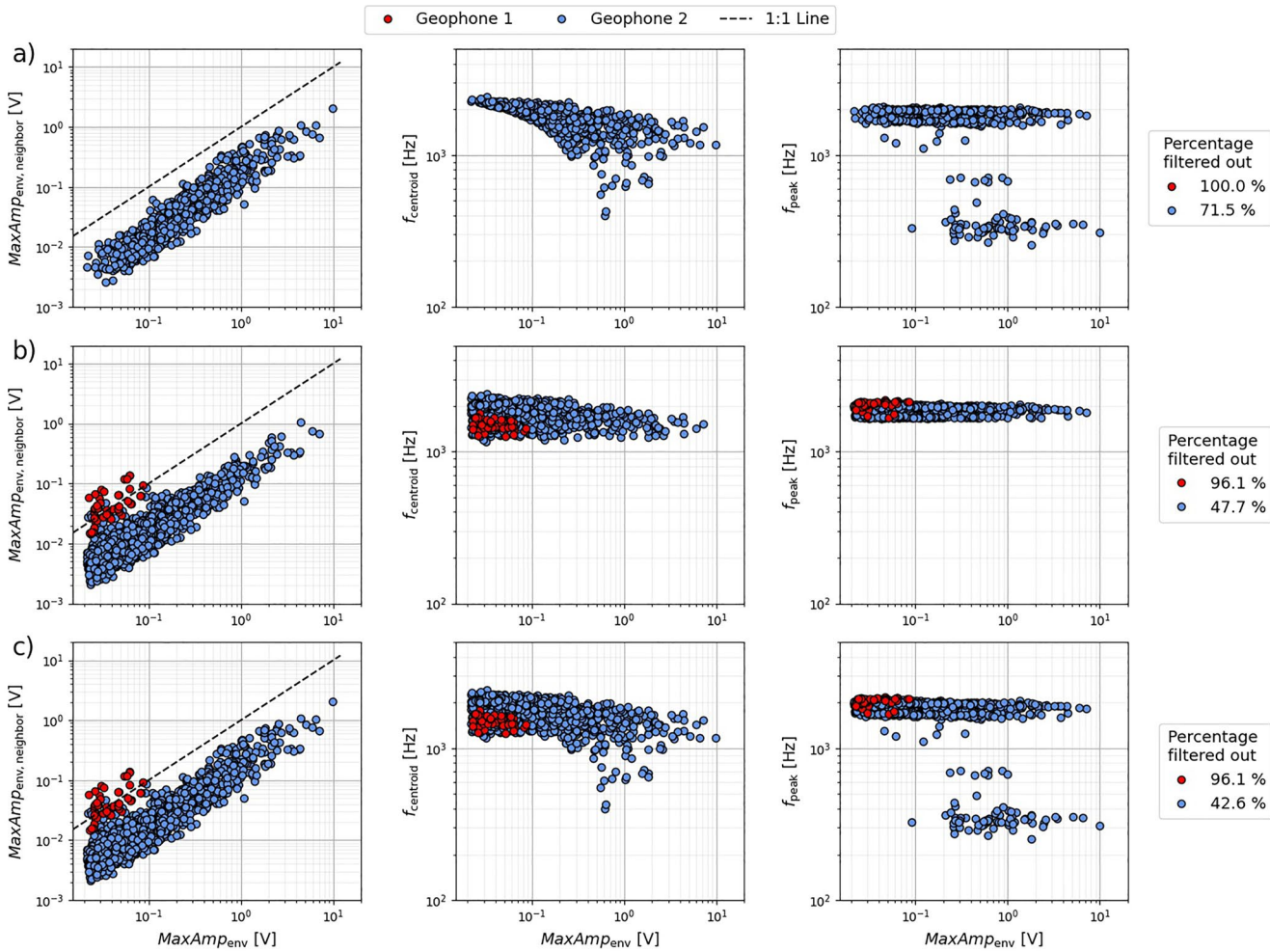

Figure 8. Attributes of the packets recorded by the shielded sensor G1 (red dots) and the unshielded sensor G2 (blue dots) that met *Criterion 1* (a), *Criterion 2* (b), and either *Criterion one* or *Criterion 2* (c) using the filter coefficients obtained for the four stations combined (see Table 4). The packet's attributes (the maximum envelope amplitude of the closest neighboring sensor plates $\mathrm{MaxAmp}_{\mathrm{env,\ neighbor}}$, the centroid frequency f_{centroid}, and the peak frequency f_{peak}) are shown as function of the maximum amplitude of each packet's envelope $\mathrm{MaxAmp}_{\mathrm{env}}$. The percentage of packets filtered out by each criterion or combination of criteria is indicated for each sensor on the right hand side.

complication is that the GSD effect on the signal response varies with the station's geometry. The wider a monitored transect is and the more plates are installed, the more apparent packets will be recorded for a given bedload mass. At the Erlenbach, almost all of the bedload is carried over only two plates because of the convex shape of the artificial stream bed. At the other sites, bedload transport is distributed over 10 to 30 plates (Table 2). Additionally, the samples collected at the Erlenbach generally have a finer GSD than at all other three sites. Finally, the flow velocity V_{w} at the Erlenbach is 1.6–3.8 times higher than at the other sites (Table 2). These differences in geometry, GSD and flow velocity may explain why the Erlenbach station records about three times fewer packets per unit mass than the three other stations, before the filter is applied (Table 5).

The filter method described in this study was developed to function similarly to the physical elastomer layer that insulates the impact plates from seismic waves generated outside of the plate boundaries. The advantage of filtering is twofold: (a) it attenuates the effect of the station's geometry and the GSD on the signal response, and (b) the remaining site-dependent factors that influence SPG signals are all measurable quantities, such as the flow velocity, the bed slope or the bed roughness.

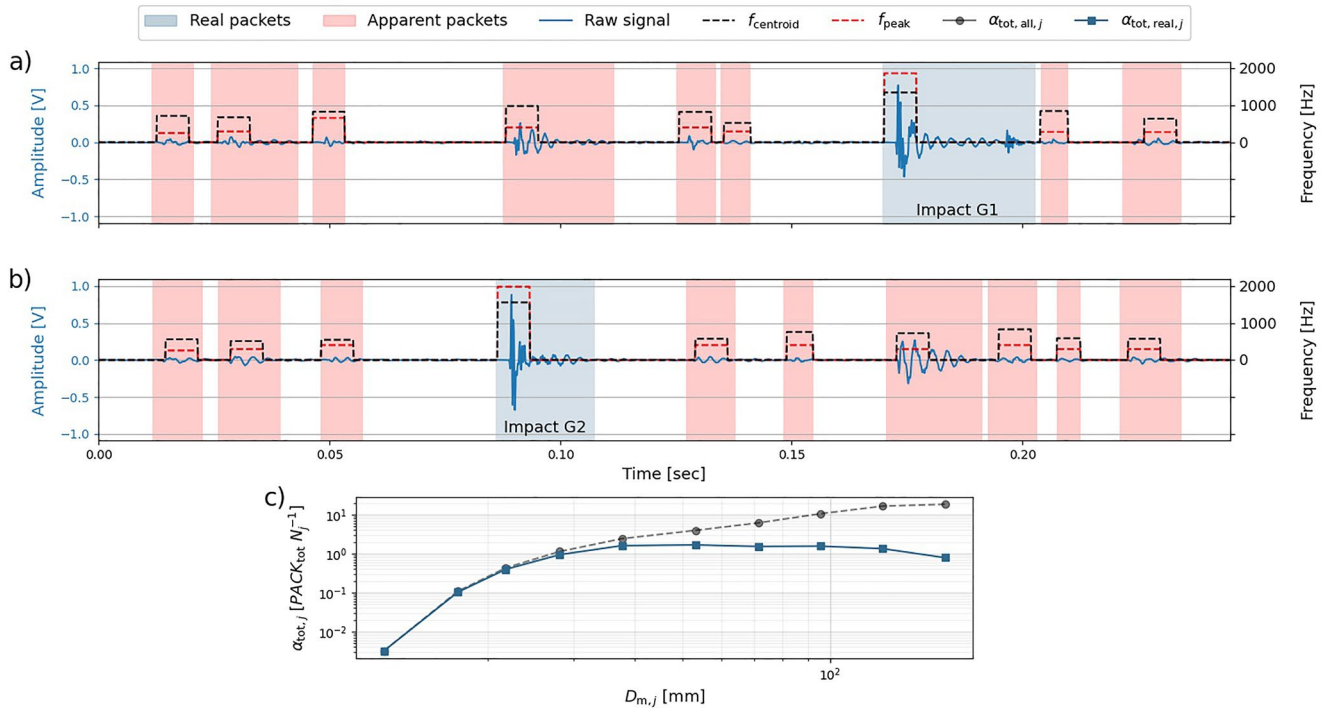

Figure 9. Raw signal recorded by the impact plates (a) G1 and (b) G2 during a single-grain-size flume experiment with particles of class $j = 6$. This figure corresponds to Figure 3, but after the application of the filter based on all 4 stations (Table 4). Real packets are marked in blue and apparent packets are marked in red. (c) Shows the change of the $\alpha_{tot,j}$ value from pre-filtering (dashed gray line, $\alpha_{tot,all,j}$) to post-filtering (solid blue line, $\alpha_{tot,real,j}$) as a function of the mean particle diameter $D_{m,j}$. Here $\alpha_{tot,all,j}$ and $\alpha_{tot,real,j}$ were calculated for each grain-size class j from the mean value over all the single-grain-size flume experiments reproducing the Albula, the Navisence, and the Avançon de Nant field sites (without the partition wall).

4.2. Field- and Flume-Based Identification of Propagating Waves

Two sources of apparent packets were identified: (a) impacts on neighboring plates and (b) impacts on the surrounding concrete bed. In Figures 3 and 4, it was shown that each source has a different seismic signature. An impact on a plate generates a wave with attributes that vary systematically as it propagates along the array of sensors, that is, the amplitude decreases and the high frequencies are progressively attenuated. By contrast, an impact on the concrete bed generates packets with similar attributes at multiple sensors. The travel path followed by the waves was hypothesized as a possible explanation for these distinct signatures. For an impact on concrete, the wave is only slightly attenuated by the dense concrete and then propagates through similar amounts of steel and elastomer at all sensor plates. This would explain the similarities in the recorded waveforms, with the only major differences between the detected packets being their starting time (Figure 4c). In the case of an impact on a plate, we hypothesize that the signal is strongly attenuated along its lateral travel path from sensor to sensor, as it repeatedly crosses the soft elastomer layer (Figure 4b).

Even though the propagation of the seismic waves is clearly visible in the field data (Figure 4), investigating their origin required flume experiments. Thanks to the video material recorded during each of these experiments, we were able to draw links between the signal response of the SPG system and the impact location. The installation of a partition wall provided a simple but efficient way to shield one plate from direct impacts and to investigate the origins of "apparent" packets. In Figures 5 and 6, impacts on the concrete are shown to generate overlapping packet characteristics at plates G1 and G2; thus isolating the plates from each other with elastomer is not sufficient to avoid the recording of apparent packets. The flume set-up was designed to replicate the flow and transport conditions during the field campaigns, including the transport of natural bedload particles (Nicollier et al., 2021). This possibly explains the good correlation between the flume and field-based density histograms of the three packet attributes used in the filter (Figure 7). Because the optimization process used to find the best filter coefficients is based only on the field data, a perfect match between the flume and field data is not required.

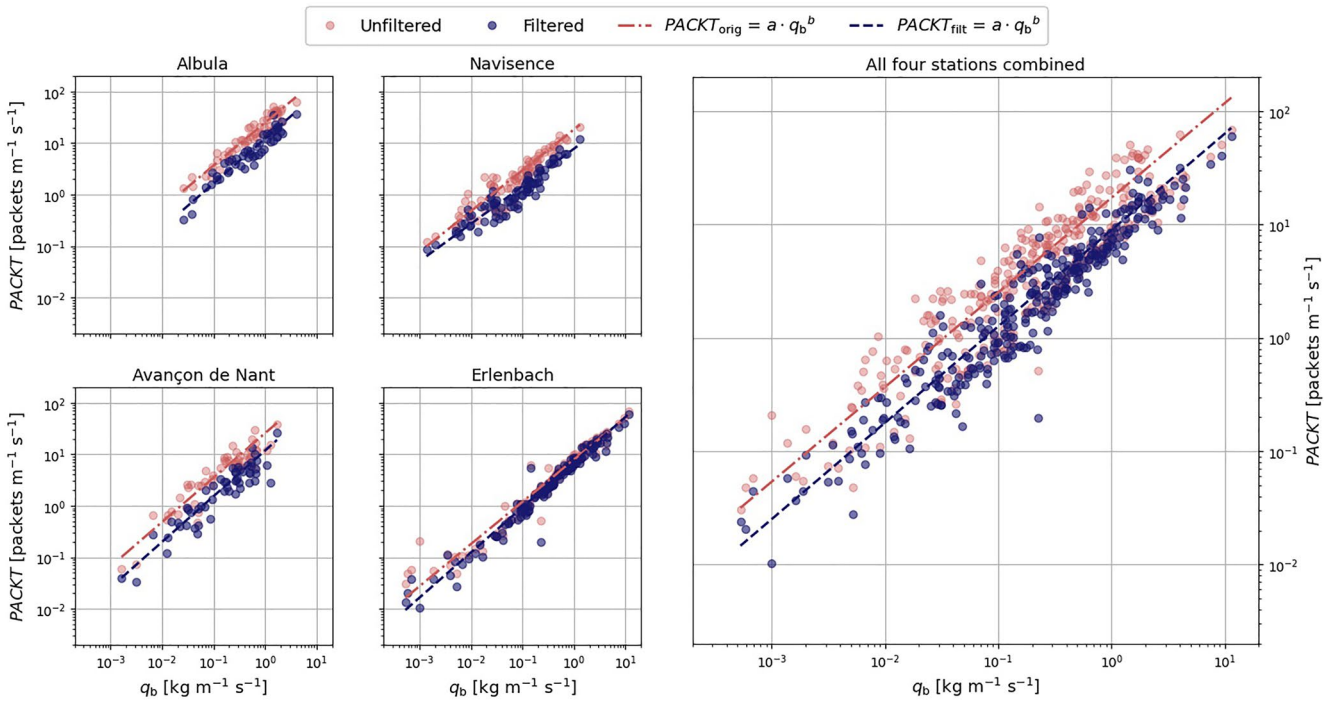

Figure 10. Total flux calibration relations linking the packet rate PACKT to the unit transport rate q_b before (red) and after filtering (blue) for each field site as well as for all four field sites combined. Each dot corresponds to one calibration measurement. The dashed lines are power-law regression lines (Equation 2); their coefficients are listed in Table 5. The filtered data was obtained using the optimal filter coefficients listed in Table 3.

Table 5
The Coefficients a and b of the Power-Law and Linear Least-Squares Regression Equations (Equation 2) for Different Field Sites Combinations

		Unfiltered			Filtered		
	Field Sites	a	b	R^2	a	b	R^2
Power-law	Albula	24.81	0.83	0.93	12.21	0.87	0.91
	Navisence	18.35	0.79	0.86	7.76	0.73	0.88
	Avançon de Nant	25.69	0.86	0.86	11.82	0.89	0.86
	Erlenbach	7.89	0.82	0.94	7.04	0.88	0.96
	3 stations[a]	24.20	0.86	0.90	11.46	0.84	0.89
	4 stations[b]	17.21	0.84	0.80	8.94	0.85	0.91
Linear least squares	Albula	28.73	1	0.87	13.65	1	0.87
	Navisence	34.92	1	0.74	18.26	1	0.67
	Avançon de Nant	35.40	1	0.80	15.35	1	0.82
	Erlenbach	10.90	1	0.88	8.62	1	0.93
	3 stations[a]	33.18	1	0.86	16.75	1	0.82
	4 stations[b]	24.93	1	0.71	12.23	1	0.85

Note. The corresponding coefficients of determination R^2 are also listed. The "filtered" coefficients were obtained from data filtered using the optimal filter parameters listed in Table 4.

[a]Includes the following three stations: Albula, Navisence, and Avançon de Nant.

[b]Includes the following four stations: Albula, Navisence, Avançon de Nant, and Erlenbach.

4.3. Filter Design

Results have shown that in order to isolate an individual plate, we must discriminate recordings generated by actual grain impacts on the plate from recordings generated by elastically propagating seismic waves resulting from impacts away from the plate. The filtering procedure developed in this paper attempts to perform this discrimination using only amplitude and frequency information, for two main reasons. First, the flume experiments with the partition wall showed that this information can be used to distinguish real from apparent packets (Figures 5 and 6). Second, extracting this information from the packets is computationally efficient, which is crucial to avoid any data loss from overloading the buffer memory.

The filter was designed to encompass most impact cases. *Criterion 1*, with its amplitude-ratio coefficient p_1 of around 1.5 and its exponential $f_{centroid}$ threshold line (Table 4, Figures 7 and 8), identifies the most obvious real packets. *Criterion 2* is meant as a complementary filter element that classifies packets with less distinct characteristics. These could be apparent packets generated by impacts on the concrete, often resulting in a $MaxAmp_{env}$/$MaxAmp_{env,\ neighbor}$ ratio close to 1 and low f_{peak} values. Furthermore, due to the stochastic nature of bedload transport, a particle can impact onto any point on a plate (Turowski et al., 2013). Particles impacting close to a neighboring plate will often yield $MaxAmp_{env}/MaxAmp_{env,\ neighbor}$ ratios close to 1, making it difficult to correctly classify the resulting packets. In order to include these real packets in the calibration, we forced the filter coefficient p_2 to be lower than 1, and filtered the packets based on their f_{peak} value. f_{peak} values larger than 1,500 Hz were found to be characteristic for real packets in most cases and this for a large range of grain sizes (Figure 6c). This characteristic of real packets probably results from the travel path of the elastic wave, which does not propagate through the dampening elastomer layer before reaching the geophone sensor. *Criterion 2* also covers the few cases where the real packet has a ratio of $MaxAmp_{env}/MaxAmp_{env,\ neighbor}$ lower than 1 but a high frequency content (e.g., when two distinct particles impact close enough in time on two different plates). We hypothesize that the probability of overlapping packets increases together with the transport rate. Finally, the slightly larger tolerance of *Criterion 2* with regard to apparent packets (Figure 8b) is, in our opinion, negligible because all the missed apparent packets had an amplitude smaller than 0.1 V. Including them in the calibration procedure would therefore have only little effect on the resulting calibration relationship for total load. A quantitative evaluation of the relevance of each criterion can be found in the Supporting Information (Tables S1 and S2 in Supporting Information S1).

The general structure of the filter was defined from results of the flume experiments that included the partition wall (Figure 6). However, the optimal coefficients were derived using field data only, in order to account for site-to-site differences in flow and transport conditions as well as station geometries. These site-specific characteristics could explain the (limited) variability in the coefficients listed in Table 4. Yet, given the wide ranges covered by the frequency attributes, the f_{peak} and $f_{centroid}$ thresholds differ only slightly from each other. Another encouraging result lies in the optimized $f_{centroid}$ threshold lines shown in Figure 7 (column 2), which approximately follow the upper border of the apparent packet characteristics for G1 in Figure 6b.

4.4. Application of the Filter to Field and Flume Data

Before addressing the results from the filtering of field and flume data, it is necessary to go one step back and discuss the meaning of the calibration. Whether we calibrate a SPG system installed at a field site or in the flume, the procedure is the same. Using Equation 2, we relate the number of detected packets to the bedload mass that was either sampled with the basket or transported in the flume over a given time interval. Additionally, we can use the $\alpha_{tot,j}$ coefficient (Equation 5) to define the detectability of particles. Applying the filtering method reduces the number of packets per particle (e.g., Figure 9c), which would imply less accurate calibration relationships. The $\alpha_{tot,j}$ values observed for the single-grain-size experiments after filtering (Figure 9c) suggest that filtering roughly equalizes the detectability of the seven largest particle classes, with unfiltered data yielding greater numbers of "apparent" packets as particle size increases. Two further observations support the efficacy of the filter method. First, the differences between $\alpha_{tot,all,j}$ and $\alpha_{tot,real,j}$ in Figure 9c correlate with the $PACK_{G1}/PACK_{tot}$ ratios in Table 3, that is, the classes for which filtering strongly reduced the number of packets were also the classes that yielded many apparent packets in the flume experiments using the partition wall. Second, the R^2 values obtained for the site-specific calibration relationships changed only slightly after the filter was applied, even though doing so

removed half of the packets (Table 5). Including apparent packets in the calibration will therefore influence the calibration relationship for a given station, but not necessarily reduce its accuracy.

The main purpose of the filter is to diminish the effect of the station geometry on the signal response. The comparison of the linear coefficient a for the stations listed in Table 5 shows that removing apparent packets significantly reduces the differences among the site-specific calibration relationships. However, after filtering, the Erlenbach station still records fewer packets per unit mass than the other three sites, likely for the following reasons. First, the high flow velocity V_w measured at the Erlenbach, may allow more particles to hop over the array of SPG plates than at the other sites (Section 4.1). Second, after having noticed the site-to-site differences visible in Figure 7 (column 1), we computed the mean $MaxAmp_{env}$-$MaxAmp_{env,neighbor}$ ratio for each station, obtaining 4.0 for the Albula, 4.2 for the Navisence, 4.8 for the Avançon de Nant and 9.3 for the Erlenbach. This result suggests that the plates at the Erlenbach are particularly well isolated from their surroundings. Note that the Erlenbach station is equipped with the first version of the SPG system, which differs slightly from the SPG system installed at the other sites. The watertight casing for the geophone and both the type and the positioning of the screws holding the plate are somewhat different. Third, the application of the filter method to the flume experiments conducted with the partition wall (Figure 8), has shown that *Criterion 2* does not eliminate all the packets detected by the shielded geophone plate G1. This possibly explains why the $\alpha_{tot,real,j}$ values of the larger grain-size classes in Figure 9c are greater than 1. Yet, this would have only a limited impact at the Erlenbach station, since we saw that the SPG system installed there is less prone to recording apparent packets for a set of reasons.

The most encouraging result from the filtering is certainly the improvement of the coefficient of determination R^2 of the global calibration relationship valid across all four sites from 0.80 to 0.91. Applying an individual filter to each site also reduces the variability of the a coefficient for linear calibrations ($b = 1$), with a varying by a factor of only 2.12 (Table 5). We can therefore conclude that (a) "apparent" packets arise primarily from seismic wave propagation, (b) filtering out these "apparent" packets yields a more consistent model among all four sites but does not significantly improve the accuracy of site-specific calibration relationships, and (c) the most effective filters will be those based on site-specific calibrations, because the effects of seismic wave propagation vary among SPG sites.

5. Conclusion

The SPG is a bedload surrogate monitoring system that has been installed in several gravel bed streams and calibrated using direct sampling techniques. In this study, video recordings of controlled flume experiments and raw data recorded at bedload monitoring stations in the field both confirm the findings from Antoniazza et al. (2020) that the SPG system is biased by seismic waves propagating through the apparatus. These waves were found to originate from particles impacting either on the surrounding concrete sill or on neighboring plates. Flume setups replicated natural transport conditions, but with the addition of a partition wall to shield one plate from impacts. Single-grain-size experiments were performed to characterize the "apparent" packets, that is, packets generated by impacts occurring beyond an individual plate, and to design a filter that identifies and removes these packets. The experiments confirmed that larger particles generated larger numbers of apparent packets. Amplitude and frequency patterns arising from the flume experiments suggest that packet characteristics can be used to distinguish real from apparent packets. The findings of these single-grain-size flume experiments were used to design a filter method, which was subsequently optimized using field data. Applying this filter results in more consistent calibration relationships among the different sites. It also facilitates the derivation of a single calibration relationship that yields reasonable estimates of the bedload transport rates measured during the calibration campaigns at all four field sites. These findings suggest that the filter method could also potentially improve estimates of fractional transport rates, particularly for the smaller grain-size fractions. Seismic waves are attenuated by their propagation through an SPG installation, so apparent packets will mostly have small amplitudes that would be mistakenly attributed to small particles. Removing these apparent packets could therefore improve SPG estimates of transport rates for smaller size fractions in grain-size mixtures. Removing apparent packets also clarifies how site-specific factors (e.g., flow velocity, bed slope, and bed roughness) influence transport rate estimates from SPG systems. Preliminary results also suggest that this filter may improve estimates of the spatial distribution of bedload transport along transects of SPG plates. In the future, packet classification based on this filter could be used to build a labeled data set on which machine learning algorithms could be trained to potentially further

improve the transport estimates. More generally, this study highlights the importance of insulating sensors as much as possible from surrounding noise sources, or correcting for the resulting signal contamination.

Conflict of Interest

The authors declare no conflicts of interest relevant to this study.

Data Availability Statement

All data presented in this paper is available online on the EnviDat repository https://www.envidat.ch/#/metadata/sediment-transport-observations-in-swiss-mountain-streams.

Acknowledgments
This study was supported by the Swiss National Science Foundation, Grant 200021L_172606, and by the Deutsche Forschungsgemeinschaft, grant RU 1546/7–1. The authors warmly thank Norina Andres, Mehdi Mattou, Nicolas Steeb, Florian Schläfli, Konrad Eppel and Jonas von Wartburg for their great help during the field calibration campaigns. They are also grateful to Michael Herkenroth of the TU Munich and the whole staff of the Oskar von Miller Institute for helping to set up and perform the flume experiments. Lorenz Ammann and Alexandre Badoux are further thanked for their valuable suggestions regarding an earlier version of the manuscript.

References

Ammon, C. J., Velasco, A. A., Thorne Lay, T., & Wallace, T. C. (2020). An overview of earthquake and seismic-wave mechanics. In C. J. Ammon, A. A. Velasco, T. Thorne Lay, & T. C. Wallace(Eds.), *Foundations of modern global seismology* (Vol. 2, pp. 39–63). Academic Press. https://doi.org/10.1016/B978-0-12-815679-7.00009-4

Ancey, C. (2020). Bedload transport: A walk between randomness and determinism. Part 2. Challenges and prospects. *Journal of Hydraulic Research*, *58*(1), 18–33. https://doi.org/10.1080/00221686.2019.1702595

Anthony, R. E., Aster, R. C., Ryan, S., Rathburn, S., & Baker, M. G. (2018). Measuring mountain river discharge using seismographs emplaced within the hyporheic zone. *Journal of Geophysical Research: Earth Surface*, *123*(2), 210–228. https://doi.org/10.1002/2017JF004295

Antoniazza, G., Nicollier, T., Boss, S., Mettra, F., Badoux, A., Schaefli, B., et al. (2022). Hydraulogical drivers of bedload transport in an Alpine watershed. *Water Resources Research*, *58*(3), e2021WR030663. https://doi.org/10.1029/2021WR030663

Antoniazza, G., Nicollier, T., Wyss, C. R., Boss, S., & Rickenmann, D. (2020). Bedload transport monitoring in alpine rivers: Variability in Swiss plate geophone response. *Sensors*, *20*(15), 4089. https://doi.org/10.3390/s20154089

Badoux, A., Andres, N., & Turowski, J. M. (2014). Damage costs due to bedload transport processes in Switzerland. *Natural Hazards and Earth System Sciences*, *14*(2), 279–294. https://doi.org/10.5194/nhess-14-279-2014

Barrière, J., Krein, A., Oth, A., & Schenkluhn, R. (2015). An advanced signal processing technique for deriving grain size information of bedload transport from impact plate vibration measurements. *Earth Surface Processes and Landforms*, *40*(7), 913–924. https://doi.org/10.1002/esp.3693

Barrière, J., Oth, A., Hostache, R., & Krein, A. (2015). Bed load transport monitoring using seismic observationsin a low-gradient rural gravel bedstream. *Geophysical Research Letters*, *42*(7), 2294–2301. https://doi.org/10.1002/2015GL063630

Blöschl, G., Kiss, A., Viglione, A., Barriendos, M., Böhm, O., Brázdil, R., et al. (2020). Current European flood-rich period exceptional compared with past 500 years. *Nature*, *583*(7817), 560–566. https://doi.org/10.1038/s41586-020-2478-3

Bogen, J., & Møen, K. (2003). *Bed load measurements with a new passive acoustic sensorErosion and sediment transport measurement in rivers: Trends and explanation*, (Vol. 283, pp. 181–182). IAHS Publications.

Bunte, K., Abt, S. R., Potyondy, J. P., & Ryan, S. E. (2004). Measurement of coarse gravel and cobble transport using a portable bedload trap. *Journal of Hydraulic Engineering*, *130130*(9), 8799–8893. https://doi.org/10.1061/(ASCE)0733-9429

Camenen, B., Jaballah, M., Geay, T., Belleudy, P., Laronne, J. B., & Laskowski, J. P. (2012). Tentative measurements of bedload transport in an energetic alpine gravel bed river. In R. M. Muñoz(Ed.), *River flow 2012*. CRC Press.

Choi, J. H., Jun, K. W., & Jang, C. D. (2020). Bed-load collision sound filtering through separation of pipe hydrophone frequency bands. *Water*, *12*(7), 1875. https://doi.org/10.3390/w12071875

Conevski, S., Winterscheid, A., Ruther, N., Guerrero, M., & Rennie, C. (2018). Evaluation of an acoustic Doppler technique for bed-load transport measurements in sand-bed Rivers. *E3S Web of Conferences*, 40, 02053. https://doi.org/10.1051/e3sconf/20184002053

Dell'Agnese, A., Mao, L., & Comiti, F. (2014). Calibration of an acoustic pipe sensor through bedload traps in a glacierized basin. *Catena*, *121*, 222–231. https://doi.org/10.1016/j.catena.2014.05.021

Dietze, M., Lagarde, S., Halfi, E., Laronne, J. B., & Turowski, J. M. (2019). Joint sensing of bedload flux and water depth by seismic data inversion. *Water Resources Research*, *55*(11), 9892–9904. https://doi.org/10.1029/2019WR026072

Einstein, H. A. (1937). *The Bedload Transport as Probability ProblemMitteilung der Versuchsanstalt für Wasserbau an der Eidgenössischen Technischen Hochschule*. Zürich.

Ferguson, R. I. (1986). River loads underestimated by rating curves. *Water Resources Research*, *22*(1), 74–76. https://doi.org/10.1029/WR022i001p00074

FOEN. (Ed.), (2021). Effects of climate change on Swiss water bodies. Hydrology, water ecology and water management. *Environmental studies. (No. 2101)* (p. 125). Federal Office for the Environment FOEN, Bern.

Geay, T., Belleudy, P., Gervaise, C., Habersack, H., Aigner, J., Kreisler, A., et al. (2017). Passive acoustic monitoring of bedload discharge in a large gravel bed river: Acoustic monitoring of bedload transport. *Journal of Geophysical Research: Earth Surface*, *122*(2), 528–545. https://doi.org/10.1002/2016JF004112

Gimbert, F., Fuller, B. M., Lamb, M. P., Tsai, V. C., & Johnson, J. P. L. (2019). Particle transport mechanics and induced seismic noise in steep flume experiments with accelerometer-embedded tracers. *Earth Surface Processes and Landforms*, *44*(1), 219–241. https://doi.org/10.1002/esp.4495

Goupillaud, P., Grossmann, A., & Morlet, J. (1984). Cycle - octave and related transforms in seismic signal analysis. *Geoexploration*, *23*(1), 85–102. https://doi.org/10.1016/0016-7142(84)90025-5

Gray, J. R., Laronne, J. B., & Marr, J. D. G. (Eds.), (2010). *Bedload-surrogate monitoring technologies, US geological survey scientific investigations report, 2010–5091*. US Geological Survey. Retrieved from http://pubs.usgs.gov/sir/2010/5091/

Habersack, H., Kreisler, A., Rindler, R., Aigner, J., Seitz, H., Liedermann, M., & Laronne, J. B. (2017). Integrated automatic and continuous bedload monitoring in gravel bed rivers. *Geomorphology*, *291*, 80–93. https://doi.org/10.1016/j.geomorph.2016.10.020

Habersack, H., Seitz, H., & Laronne, J. B. (2008). Spatio-temporal variability of bedload transport rate: Analysis and 2D modelling approach. *Geodinamica Acta*, *21*(1–2), 67–79. https://doi.org/10.3166/ga.21.67-79

Halfi, E., Paz, D., Stark, K., Yogev, U., Reid, I., Dorman, M., & Laronne, J. B. (2020). Novel mass-aggregation-based calibration of an acoustic method of monitoring bedload flux by infrequent desert flash floods. *Earth Surface Processes and Landforms*, *45*(14), 3510–3524. https://doi.org/10.1002/esp.4988

Harper, W. V. (2014). *Reduced Major Axis Regression: Teaching Alternatives to Least Squares* (Vol. 24). Mathematics Faculty Scholarship. Retrieved from https://digitalcommons.otterbein.edu/math_fac/24

Helley, E. J., & Smith, W. (1971). *Development and calibration of a pressure-difference bedload sampler*. US Department of the Interior, Geological Survey, Water Resources Division.

Hilldale, R. C., Carpenter, W. O., Goodwiller, B., Chambers, J. P., & Randle, T. J. (2015). Installation of impact plates to continuously measure bed load: Elwha River, Washington, USA. *Journal of Hydraulic Engineering*, *141*(3), 06014023. https://doi.org/10.1061/(ASCE)HY.1943-7900.0000975

Johnson, K. (1985). *Contact mechanics*. Cambridge University Press. https://doi.org/10.1017/CBO9781139171731

Jones, E., Oliphant, T., & Peterson, P. (2002). *SciPy: Open source scientific tools for Python [cited 2021 June 16]*. Retrieved from http://www.scipy.org

Koshiba, T., Auel, C., Tsutsumi, D., Kantoush, S. A., & Sumi, T. (2018). Application of an impact plate – bedload transport measuring system for high-speed flows. *International Journal of Sediment Research*, *33*(1), 35–46. https://doi.org/10.1016/j.ijsrc.2017.12.003

Koshiba, T., & Sumi, T. (2018). Application of the wavelet transform to sediment grain sizes analysis with an impact plate for bedload monitoring in sediment bypass tunnels. *E3S Web of Conferences*, *40*, 04022. https://doi.org/10.1051/e3sconf/20184004022

Krein, A., Klinck, H., Eiden, M., Symader, W., Bierl, R., Hoffmann, L., & Pfister, L. (2008). Investigating the transport dynamics and the properties of bedload material with a hydro-acoustic measuring system. *Earth Surface Processes and Landforms*, *33*(1), 152–163. https://doi.org/10.1002/esp.1576

Kreisler, A., Moser, M., Aigner, J., Rindler, R., Tritthard, M., & Habersack, H. (2017). Analysis and classification of bedload transport events with variable process characteristics. *Geomorphology*, *291*, 57–68. https://doi.org/10.1016/j.geomorph.2016.06.033

Kristeková, M., Kristek, J., Moczo, P., & Day, S. M. (2006). Misfit criteria for quantitative comparison of seismograms. *Bulletin of the Seismological Society of America*, *96*(5), 1836–1850. https://doi.org/10.1785/0120060012

Kuhnle, R., Wren, D., Hilldale, R. C., Goodwiller, B., & Carpenter, W. (2017). Laboratory calibration of impact plates for measuring gravel bed load size and mass. *Journal of Hydraulic Engineering*, *143*(12), 06017023. https://doi.org/10.1061/(ASCE)HY.1943-7900.0001391

Le Guern, J., Rodrigues, S., Geay, T., Zanker, S., Hauet, A., Tassi, P., et al. (2021). Relevance of acoustic methods to quantify bedload transport and bedform dynamics in a large sandy-gravel-bed river. *Earth Surface Dynamics*, *9*(3), 423–444. https://doi.org/10.5194/esurf-9-423-2021

Mao, L., Carrillo, R., Escauriaza, C., & Iroume, A. (2016). Flume and field-based calibration of surrogate sensors for monitoring bedload transport. *Geomorphology*, *253*, 10–21. https://doi.org/10.1016/j.geomorph.2015.10.002

Mizuyama, T., Laronne, J. B., Nonaka, M., Sawada, T., Satofuka, Y., Matsuoka, M., et al. (2010). Calibration of a passive acoustic bedload monitoring system in Japanese Mountain Rivers. In J. R. Gray, J. B. Laronne, & J. D. G. Marr(Eds.), *Bedload-surrogate monitoring technologies. US geological survey scientific investigations report, 2010–5091* (pp. 296–318). US Geological Survey. Retrieved from http://pubs.usgs.gov/sir/2010/5091/papers/listofpapers.html

Mizuyama, T., Oda, A., Laronne, J. B., Nonaka, M., & Matsuoka, M. (2010). Laboratory tests of a Japanese pipe geophone for continuous acoustic monitoring of coarse bedload. In J. R. Gray, J. B. Laronne, & J. D. G. Marr(Eds.), *Bedload-surrogate monitoring technologies. US geological survey scientific investigations report, 2010–5091* (pp. 319–335). US Geological Survey. Retrieved from http://pubs.usgs.gov/sir/2010/5091/papers/listofpapers.html

Mühlhofer, L. (1933). Untersuchungen über die Schwebstoff und Geschiebeführung des Inn nächst Kirchbichl (Tirol). *Wasserwirtschaft*, *1*(6), 23.

Nicollier, T., Rickenmann, D., Boss, S., Travaglini, E., & Hartlieb, A. (2020). Calibration of the Swiss plate geophone system at the Zinal field site with direct bedload samples and results from controlled flume experiments. In *River flow 2020* (pp. 901–909). Proceedings of the 10th Conference on Fluvial Hydraulics. https://doi.org/10.1201/b22619

Nicollier, T., Rickenmann, D., & Hartlieb, A. (2021). Field and flume measurements with the impact plate: Effect of bedload grain-size distribution on signal response. *Earth Surface Processes and Landforms*, *46*(8), 17–1520. https://doi.org/10.1002/esp.5117

Raven, E. K., Lane, S. N., & Ferguson, R. (2010). Using sediment impact sensors to improve the morphological sediment budget approach for estimating bedload transport rates. *Geomorphology*, *119*(1–2), 125–134. https://doi.org/10.1016/j.geomorph.2010.03.012

Reid, I., Frostick, L. E., & Layman, J. T. (1985). The incidence and nature of bedload transport during flood flows in coarse-grained alluvial channels. *Earth Surface Processes and Landforms*, *10*(1), 33–44. https://doi.org/10.1002/esp.3290100107

Rickenmann, D. (2017). Bed-load transport measurements with geophones and other passive acoustic methods. *Journal of Hydraulic Engineering*, *143*(6), 03117004. https://doi.org/10.1061/(ASCE)HY.1943-7900.0001300

Rickenmann, D., & Fritschi, B. (2017). Bedload transport measurements with impact plate geophones in two Austrian mountain streams (fischbach and ruetz): System calibration, grain size estimation, and environmental signal pick-up. *Earth Surface Dynamics*, *5*(4), 669–687. https://doi.org/10.5194/esurf-5-669-2017

Rickenmann, D., & McArdell, B. W. (2007). Continuous measurement of sediment transport in the Erlenbach stream using piezoelectric bedload impact sensors. *Earth Surface Processes and Landforms*, *32*(9), 1362–1378. https://doi.org/10.1002/esp.1478

Rickenmann, D., & McArdell, B. W. (2008). Calibration measurements with piezoelectric bedload impact sensors in the Pitzbach mountain stream. *Geodinamica Acta*, *21*(1–2), 35–52. https://doi.org/10.3166/ga.21.35-52

Rickenmann, D., Steeb, N., & Badoux, A. (2018). Improving bedload transport determination by grain-size fraction using the Swiss plate geophone recordings at the Erlenbach stream. *E3S Web of Conferences*, *40*, 02009. https://doi.org/10.1051/e3sconf/20184002009

Rickenmann, D., Turowski, J. M., Fritschi, B., Klaiber, A., & Ludwig, A. (2012). Bedload transport measurements at the Erlenbach stream withgeophones and automated basket samplers. *Earth Surface Processes and Landforms*, *37*(9), 1000–1011. https://doi.org/10.1002/esp.3225

Rickenmann, D., Turowski, J. M., Fritschi, B., Wyss, C., Laronne, J. B., Barzilai, R., et al. (2014). Bedload transport measurements with impact plate geophones: Comparison of sensor calibration in different gravel-bed streams. *Earth Surface Processes and Landforms*, *39*(7), 928–942. https://doi.org/10.1002/esp.3499

Roth, D. L., Brodsky, E. E., Finnegan, N. J., Rickenmann, D., Turowski, J. M., & Badoux, A. (2016). Bed load sediment transport inferred from seismic signals near a river. *Journal of Geophysical Research: Earth Surface*, *121*(4), 725–747. https://doi.org/10.1002/2015JF003782

Stoffel, M., Tiranti, D., & Huggel, C. (2014). Climate change impacts on mass movements - case studies from the European Alps. *The Science of the Total Environment*, *493*, 1255–1266. https://doi.org/10.1016/j.scitotenv.2014.02.102

Thorne, P. D. (1986). Laboratory and marine measurements on the acoustic detection of sediment transport. *Journal of the Acoustical Society of America*, *80*(3), 899–910. https://doi.org/10.1121/1.393913

Turowski, J. M., Bockli, M., Rickenmann, D., & Beer, A. (2013). Field measurements of the energy delivered to the channel bed by moving bed load and links to bedrock erosion. *Journal of Geophysical Research: Earth Surface*, *118*(4), 2438–2450. https://doi.org/10.1002/2013JF002765

Wales, D. J., & Doye, J. P. K. (1997). Global optimization by basin-hopping and the lowest energy structures of Lennard-Jones clusters containing up to 110 atoms. *Journal of Physical Chemistry A*, *101*(28), 5111–5116. https://doi.org/10.1021/jp970984n

Wyss, C. R., Rickenmann, D., Fritschi, B., Turowski, J., Weitbrecht, V., & Boes, R. (2016a). Laboratory flume experiments with the Swiss Plate Geophone bed load monitoring system: 1. Impulse counts and particle size identification. *Water Resources Research*, *52*(10), 7744–7759. https://doi.org/10.1002/2015WR018555

Wyss, C. R., Rickenmann, D., Fritschi, B., Turowski, J., Weitbrecht, V., & Boes, R. (2016c). Measuring bed load transport rates by grain-size fraction using the Swiss plate geophone signal at the Erlenbach. *Journal of Hydraulic Engineering*, *142*(5), 04016003. https://doi.org/10.1061/(ASCE)HY.1943-7900.0001090

Wyss, C. R., Rickenmann, D., Fritschi, B., Turowski, J., Weitbrecht, V., Travaglini, E., et al. (2016b). Laboratory flume experiments with the Swiss Plate Geophone bed load monitoring system: 2. Application to field sites with direct bed load samples. *Water Resources Research*, *52*(10), 7760–7778. https://doi.org/10.1002/2016WR019283

Reference From the Supporting Information

Nicollier, T., Rickenmann, D., & Hartlieb, A. (2019). *Field calibration of the Swiss plate geophone system at the Albula stream and comparison with controlled flume experiments* (p. 8). Paper presented at the SEDHYD 2019 Conference.